Annealing study in oxygen environment of Iron (Fe) and Nickel (Ni) thin films

Megha Chacko Kachappilly

Master of Science (by Research)

University of York

Department of Physics

April 2023

Abstract

Metals, ceramics, and polymers are just a few of the materials that can be used with thin film technology. The majority of early material science research was primarily concerned with well-defined metals but, as a result of the various important industrial uses of metal oxide systems, there has been a phenomenal increase in this area of study. To tailor the physical properties of metal-metal oxide films placed onto ceramic substrates for specific purposes, it is essential to understand how growth and/or annealing conditions affect the crystallography and microstructure of the films.

In order to study the differences in the growth of single and polycrystalline structures, as well as, to understand the impact of annealing on the surface morphology and structure of the films, Fe and Ni films were grown epitaxially on a MgO(001) substrate using the molecular beam epitaxy (MBE) technique and were annealed in-situ in the MBE chamber under a controlled temperature of 400ºC and oxygen partial pressure of 5×10^{-6} mbar. Reflection high-energy electron diffraction (RHEED), transmission electron microscopy (TEM), scanning electron microscopy (SEM) / energy-dispersive x-ray spectroscopy (EDS), and atomic force microscopy (AFM) techniques were used to characterise the structure of the films.

According to the structural analyses, Fe films grew on the MgO(001) substrate with more uniformity than Ni films. Comparing Ni films to Fe films, higher surface roughness was visible on Ni film, which is possibly due to the larger mismatch (~16%) between Ni film and MgO substrate. The analysis of annealed film lattice shows that the films get oxidised and RMS surface roughness increased with annealing. The lattice d-spacing analysis, from high-resolution TEM (HRTEM) images and selected area electron diffraction (SAED) pattern on the annealed samples, indicated that the Fe films were half oxidised towards Fe_3O_4 (magnetite) along with non-oxidised iron and Ni films were fully oxidised to NiO.

Contents

List of Tables

List of Figures

Acknowledgement

I would like to express my sincere gratitude to my supervisor Prof Vlado Lazarov for giving me the opportunity to be a part of his research group. His deep passion for physics is always an inspiration to me. I thank him for his guidance and endless support.

I am extremely grateful to my Co-Supervisor Dr Leonardo Lari for his tireless guidance throughout this project. I thank him for supporting me with microscopy (TEM, SEM/EDS) training and data analysis. It was an immense pleasure to work with him and I thank him once again for being a kind and encouraging person all the time.

Further acknowledgement and thanks go to the postdoc of my group, Dr Adam Kerrigan and PhD student, Mr Ahmad Althumali who helped me with the growth of thin films using MBE and instrument training on AFM.

I would also like to thank other PhD students whom I have shared my journey with, especially Miss Fayzah Talbi who has helped me in learning the Manual polishing and PIPS of the cross-section samples for TEM analysis. I thank all my colleagues for their assistance. Their advice made my journey easy and less stressful.

Finally, I would like to thank my family for their unconditional love and support.

Declaration

I humbly declare that this thesis submitted to the University of York is a presentation of my own research, and has not been previously submitted for any award in this or any other university. All sources are acknowledged as references.

Chapter 1
Introduction

In the current era of science and technology, material science plays an essential part. To suit commercial and individual needs, a variety of materials are utilised in industry, housing, agriculture, transportation, etc. Numerous opportunities have been created for better knowledge and application of various materials as a result of rapid advancements in the field of solid-state physics. Thousands of materials, such as metals, ceramics, polymers, composites, semiconductors, biomaterials, and advanced materials are readily available; however, choosing the right material for a given application is a highly difficult task. The best choice of materials may be made, nevertheless, by having a solid understanding of the fundamental properties of the various materials [1, 2].

1.1 Metal oxides

Most of the early material science research was focused on metals but, as a result of the numerous significant technological applications of metal oxide systems, there has been an incredible surge in this field of study. The class of materials known as metal oxides is broad and interesting, with characteristics ranging from metals to semiconductors and insulators. These materials are earth-abundant and their variety of features enables them to be used in applications ranging from energy storage to catalysis [3]. The stability of electrode/electrolyte interfaces in fuel cells, the failure of dielectric materials due to surface conductivity, catalysts for the partial oxidation of hydrocarbons, spintronic-based storage devices, solid-state gas sensors for pollution monitoring and control, and the passivation of metal surfaces against corrosion are all dependent on the characteristics of metal-oxide surfaces or the interface between metal oxides and other materials.

Comparatively speaking, the study of metal-oxide surfaces lags behind that of metals and semiconductors. This makes studying oxide surfaces more difficult for a number of reasons. The level of complexity is a significant issue. When it comes to crystal structures, this is obvious. Finding out where the atoms are on a surface is one of the initial objectives of a structural investigation, but it is obvious that the complexity of oxide structures can make this a difficult task. In reality, there are surprisingly few oxide surface structures that have been accurately identified. A complex combination of chemical and physical properties goes along with complicated crystallography. Numerous elements, particularly transitional metals, exhibit a variety of potential oxidation states, leading to a number of oxides with various compositions. For surface research, this chemical

complexity has a wide range of important impacts. Surface defects are definitely an essential component of metal oxides and their characteristics.

It is acknowledged that the existence of surface imperfections frequently causes catalytic activity. Anion or cation vacancies, which have an impact on the site's electronic energy levels, are a common defect on oxide surfaces. Oxide vacancies occur more frequently than metal cation vacancies. Other defects that metal oxides may have include steps, kinks, and impurity atoms, which are comparable to those that are present on elemental surfaces. For all material science experiments, surface preparation is a crucial component. The creation of virtually perfect surfaces for any alloy is challenging compared to the fabrication of elemental solids. The process of cleaving in an ultrahigh vacuum (UHV) is maybe the greatest way to create nearly perfect surfaces [4].

Additionally, material scientists have the choice of creating thin films of the oxide in situ on an appropriate substrate, or using commercially available single crystals that have been cleaved to disclose the appropriate surface orientation, for undertaking more fundamental experiments. It is possible to create thin films on suitable metal substrates, which are sufficient to replicate the surfaces of bulk terminated crystals, rather than analysing bulk metal oxide crystals. Either direct metal oxide deposition or metal deposition followed by oxidation can be used to grow the oxide film.

1.1.1 Applications of Metal Oxides

Metal oxides as catalysts

Metal oxide catalytic materials are being used extensively in the chemical, environmental, and petroleum industries. They include simple oxides like silica, alumina, clays, zeolites, titania, zirconia, and ZnO as well as complex oxides like porous and mesoporous metal oxides. The majority of commercial catalysts are composed of metal deposits on a metal oxide substrate with a high surface area. In some instances, the metal oxides themselves can operate as catalysts, either in pure forms (such as bismuth molybdate in the synthesis of acrylonitrile) or mixed forms (such as V_2O_5 on TiO_2 in the selective oxidation of hydrocarbons and selective catalytic reduction of NO_x) [5, 6].

The chemical industries make considerable use of metal oxides as catalysts for selective oxidation in the creation of chemical intermediaries. These metal oxides have particular characteristics like acidity, basicity, and redox aspects, which result in particular catalytic properties. The surface of an oxide may have different defects and environments (kinks, steps, terraces), which could affect the catalytic

phenomena, such as making metal oxides more susceptible to catalytic processes due to their structural characteristics [6].

Fe_3O_4 is utilised as an iron source in catalysts in the "Haber-Bosch method," a chemical reaction that improves the reactivity of nitrogen and hydrogen to produce ammonia. This process is currently the most popular process for producing ammonia on a wide scale [7]. In numerous synthetic transformations, such as oxidative addition, C-H activation, reductive elimination, oxidative cyclization, oligomerization, and the creation of carbon-carbon and carbon-heteroatom bonds in cross-coupling processes, Ni serves as a key catalyst. In cross-coupling processes, nickel is utilised in place of palladium as a catalyst since it is less expensive than other transition metal catalysts [8, 9].

Corrosion controlling

Corrosion is the ongoing degradation of a material and is caused by a number of variables, including the application environment, operating circumstances, the presence of non-equilibrium phases, the failure of protective phases or layers in the materials, etc. Materials can change during the corrosion process into a new form that may be reactive or protective in subsequent processes. The thermodynamic instability of a given material system in the combined environment and working conditions is typically the driving factor behind corrosion. Depending on the application type and corrosive environment, many ways are used to reduce or slow down the corrosion of a material system. Applying protective or non-reactive phases in the form of coatings over the material system to prevent exposure to the environment is the quickest and most popular way. Because of the stability and resistance to the diffusion of various ionic species, oxide systems are typically recognised for their protective activity. The iron-containing alloy stainless steel is a well-known example of an oxide layer-assisted corrosion-resistant alloy because the alloying element chromium (Cr) creates an unbreakable stable oxide layer (Cr_2O_3, also known as chromia) along the grain boundaries and surface. Although chromia cannot be used alone because of brittleness, chromium enhances passivity when alloyed with other metals and alloying elements in stainless steel. Another example is Aluminium (Al) and Al – alloys [10]. The invention of corrosion-resistant surface coating based on NiO also have a huge industrial application [11, 12].

Sensors

The optical, electrical, and thermal properties of metal oxide semiconductors (MOS) have made them more popular in monitoring and detecting explodes and harmful gases. SnO_2, ZnO, Fe_2O_3, TiO_2, In_2O_3, Co_3O_4, and CuO are the most

popular metal oxide semiconductor materials that have been used as sensors. Due to their inherent physical and chemical characteristics, metal oxide semiconductors have recently emerged as the preferred material to fabricate extremely sensitive, reliable, and cheap gas sensors for real-world applications [13]. SnO_2, ZnO, WO_3, and TiO_2 are examples of wide-band-gap metal oxide semiconductors whose electrical conductivity varies depending on the type of gas surrounding them. As a result, they are the most common and practical sensing materials utilised to make inexpensive gas sensing equipment [14].

Hydrogen peroxide (H_2O_2) is a chemical that is utilised in bleaching and antibacterial treatments, among other things. However, too much H_2O_2 can damage the eyes and exposed skin. In order to detect H_2O_2, it is crucial to create sensitive and precise sensors. Enzyme-based sensors are often one type of option for detecting H_2O_2. The limitations on development and applications are intricate processes, expensive costs, and unsuitability for large-scale production. It is well known that Fe_3O_4 nanoparticles have an enzyme-mimicking property that is comparable to that of natural peroxidases. Due to this special property of Fe_3O_4 and the low cost of thin-film technology, Fe_3O_4 thin films are being investigated intensively for the production of H_2O_2 sensors [15]. Numerous NiO-based gas sensors are well suited for use in applications for monitoring environmental harmful gases including carbon monoxide and nitrogen oxide due to their physical and sensing properties. These sensors also showed similar NO_2 gas-sensing properties [16, 17].

Spintronics

Conventional electronics use only the charge of charge carriers (electrons and holes). This field is well established and has some limitations in applying the next-generation spintronic devices, which use both charge and spin of the charge carriers. Many devices work based on spintronics, for e.g., storage devices, sensors, transistors, and other integrated circuits [18]. The combination of ferromagnetism and semiconducting characteristics of the single-phased or hetero-structured materials is related to Magnetic Tunnel Junction (MTJ) based spintronics, according to several research. Giant magnetoresistance (GMR), which was found in metallic multilayers (such as Fe/Cr or Co/Cu superlattices) in the 1980s, was the first spintronics phenomenon that received significant academic attention. Tunnel magnetoresistance (TMR), another spintronics phenomenon, has sparked a significant amount of experimental and theoretical research. The interest in oxides in spintronics has rapidly grown since the first ground-breaking TMR results were reported on tunnel junctions based on manganese perovskite oxides [19]. Due to their distinctive magnetic and electrical

characteristics, transition-metal oxides are regarded as potential candidates for functional spintronic materials. More recently, the growth of multiferroic materials in thin film form and the renewed interest in their properties, which typically include ferromagnetism, ferroelectricity, and ferroelasticity in single-phased or hetero (composite) structures have opened up new applications for oxides in spintronics.

Fe_3O_4 thin films have recently received a lot of attention for use in spintronic devices due to their benefits, most notably those listed below. First, Fe_3O_4 has strong spin polarisation (approximately 100%) and a high Curie temperature (around 860 K), which are typically needed in magnetoresistance (MR) fields. Second, Fe_3O_4 thin films can have their magnetic and electrical characteristics changed [15]. NiO is a potential material for spintronic devices, in which signals are carried by propagating disturbances (i.e. magnons) in the ordering of magnetic materials rather than by electrical currents [20, 21].

Metal oxides are also employed in solar cells [22], superconducting materials [23], photoactive materials [24] and dielectric materials [25].

1.2 Thin films

Although thin film techniques have been studied for well over a century, it has only been in the last few decades that they have been exploited extensively in real-world applications [26]. A thin film is a layer of material that can range in thickness from a few nanometers to several micrometres and can be described as a low-dimensional structure made by the sequential condensation of atomic, molecular, and ionic species of matter [27]. Modern technology requires thin films for various applications. Many electronic semiconductor devices such as transistors, sensors, photovoltaic devices, solar cells, light-emitting diodes, photoconductors and light crystal displays are the main applications benefiting from thin film construction. Thin films are the main drivers of ongoing technological developments in the sectors of optoelectronic, photonic, and magnetic storage devices. Due to their distinct electrical, magnetic and optical qualities, the majority of functional materials are applied in thin film form. Thin film technologies take advantage of the fact that the thickness parameter can be used to control attributes in particular. Many organisations have used a variety of deposition processes, including thermal evaporation, sputtering, molecular-beam epitaxy, pulsed laser deposition, chemical vapour deposition (CVD), dip coating, etc. to create metal oxide thin films. This study uses the MBE technique in order to guarantee minimum contamination and excellent measurement accuracy. The details of the MBE technique are discussed in chapter 2.

1.3 Aim of the present study

Thin film technology can be applied to different substrate material such as metals, ceramics or polymers. It is crucial to comprehend how the growth and/or annealing conditions affect the crystallography and microstructure of metallic films deposited onto ceramic substrates in order to tune their physical properties (such as magnetic, electrical, etc.) for particular applications.

Due to the chemical, thermal, and mechanical stability, MgO has been frequently employed as a substrate for thin metallic coatings and there has been an increase in interest in the synthesis and characterization of Fe (body-centered cubic structure) layers on MgO (rock salt structure) due to their technological uses. However, MgO and Fe (bcc) have lattice parameters of 4.212 Å and 2.87 Å, respectively. Since there is only a 4% lattice mismatch (due to a 45º rotation of Fe lattices with respect to MgO), Fe has been seen to grow on MgO(001) successfully [28-30]. Even in the presence of a lattice mismatch, a thin film can develop on a substrate as a strained epitaxial layer. At room temperature, there is a 16% lattice mismatch between Ni and MgO(001) but, numerous studies have been done on the formation of thin films of Ni (face-centered cubic structure) on MgO (rock salt structure), and Ni is predicted to interact strongly with MgO [31, 32].

The main aim of this study is to understand the self-oxidation in metallic thin films and the comparison of self-formed metal-metal oxide to metal-metal oxide structures grown by MBE, through the epitaxial growth and structural characterisation of as-grown and in situ annealed Fe & Ni thin films on MgO(001) substrate.

1.4 Magnesium Oxide - MgO(001) substrate

Since the substrate lattice serves as a template for thin film growth, substrate selection is one of the initial steps in any thin film deposition study. The precise lattice of single-crystal substrates makes them the best option for thin film deposition. For thin films of materials such as ferro magnetic, photo-electronic, and high T_C superconductors, magnesium oxide makes a great single-crystal substrate. It has the empirical formula MgO and is made up of an interlocking lattice of Mg^{2+} and O^{2-} ions that are held together by ionic bonding. MgO crystallises in the cubic Fm-3m space group and has a rock salt structure. Magnesium oxide's crystal lattice has an octahedral geometry with a lattice constant of a = 4.212 Å in which the strongly coupled Mg^{2+} and O^{2-} ions result in their high melting point [33]. It has a special ability to tolerate high temperatures, which makes it a popular refractory material in industries. The various

applications of MgO in dehydrating material [34], medicines [35], etc. make it more attractive.

1.5 Iron and Iron oxides

Iron (Fe) is the most common metal in the crust of the earth. At atmospheric pressure, iron has two distinct crystal structures: the body centered cubic (bcc) and the face centered cubic (fcc). The bcc α-phase is stable in the ground state, and at T=1184 K, α-Fe changes into the fcc γ-phase, which is stable up to 1665 K. Iron changes back into the bcc phase (δ-Fe) above this point, where it remains stable until it reaches the melting point T_m =1809 K [36]. Iron oxides, which are utilised in a variety of applications from the manufacture of steel to data storage devices, are created using iron ore as the raw material. Compounds made of iron and oxygen are known as iron oxides.

Magnetite (Fe_3O_4)

Magnetite (Fe_3O_4) is the oldest magnetic substance known to science and a frequent rock-forming iron oxide. It is a ferrimagnet with a critical temperature T_C = 858K. When Fe_3O_4 crystallises, it takes the shape of a spinel, where the A sites are occupied by Fe^{3+} ions and the B sites by a combination of Fe^{2+} and Fe^{3+} ions [19, 37]. Fe_3O_4 is particularly appealing for a variety of commercial and industrial applications because of its good epitaxial fit to technologically significant semiconductor and oxide substrates (mentioned above in section 1.1.1). Due to theoretically expected half-metallic features, such as 100% spin polarisation at the Fermi level, magnetite (Fe_3O_4) has been receiving a lot of interest.

1.6 Nickel and Nickel oxides

Nickel (Ni) is a transition metal that is hard and ductile. Despite the fact that pure nickel is chemically reactive, big pieces take longer than usual to react with air because, under normal circumstances, a passivation layer of nickel oxide grows on the surface to stop further corrosion. Nickel typically has a face-centered cubic structure with a lattice parameter of 3.52Å. Because it is corrosion-resistant, nickel is used to safeguard other metals by plating them, and it is used in the creation of alloys like stainless steel, for example. NiO can be produced when nickel powder is heated over 400°C [38].

Nickel oxide (NiO)

Nickel (II) oxide (NiO) is a basic oxide of nickel that adopts the NaCl structure, with octahedral Ni^{2+} and O^{2-} sites. It is a charge-transfer insulator that is antiferromagnetic. NiO is frequently non-stoichiometric, just like many other binary metal oxides. NiO is a fascinating material since it is used in radiation

detectors, solar cells, semiconducting devices, laser materials, thermoelectric devices, and optoelectronic devices [39].

Chapter 2
Methodology

This chapter gives an overview of the techniques used to grow and characterize thin films in this work. It includes a detailed explanation of the MBE growth and structural characterisation using electron microscopy and chemical analysis by EDS. It also cover the mechanical polishing technique for the preparation of cross-section specimens for TEM in detail.

2.1 Ultra-High Vacuum Systems

The majority of the thin film deposition techniques currently in use require a decreased pressure environment or vacuum to ensure low contamination. The level of vacuum required can be different according to the deposition techniques. Based on the deposition chamber pressure, the vacuum levels can be defined as in Table. 2.1[40].

Vacuum Level	**Pressure Range (mbar)**
Rough Vacuum	1×10^{0} to 1×10^{-3}
Low Vacuum	1×10^{-3} to 1×10^{-6}
High Vacuum	1×10^{-6} to 1×10^{-9}
Ultra-High Vacuum	$< 1 \times 10^{-9}$

Table 2. 1: Classification of vacuum levels according to the different pressure ranges [40].

This work mainly uses an UHV level which is required for the deposition of high-purity thin films.

2.1.1 Vacuum Pumps

Maintaining UHV conditions is very challenging, and this usually achieved by combining a number of vacuum pumps. Gas transfer pumps and entrapment pumps are the two main groups of vacuum pumps. Gas transfer pumps transfer gas molecules in one or more stages of compression from the pumped volume to the ambient air. Entrapment pumps force molecules to condense or chemically bond to the walls of the chamber they are pumping. Some entrapment pumps are reversible and release trapped (condensed) gas back into the system during warm-up, unlike gas transfer pumps, which permanently remove gas.

The two further categories of gas transfer pumps are positive-displacement and kinetic vacuum pumps. Positive-displacement pumps include roots pumps and rotary mechanical pumps. The two best-known kinetic vacuum pumps are diffusion and turbomolecular pumps. Adsorption, sputter-ion, and cryogenic pumps are a few of the entrapment pumps that are frequently used. In a variety of

pumping system configurations, each pump is utilised separately or in combination [41].

Rotary Mechanical Pump

The rotary mechanical pump is one of the most well-known and widely used positive displacement pumps. Typically, rotary pumps have a mounted rotor with spring-loaded vanes (see Fig. 2.1). The vanes will move in and out as the rotor rotates, allowing a volume of gas to be constrained, compressed, and eventually released via the exhaust valve. To seal and lubricate the working parts, oil is introduced to the rotary pump, but the oil itself can be a source of contamination, hence oil traps are frequently attached to pumps to reduce this danger. In a multi-vacuum system, the rotary pump is widely applied as the first stage because of its ability to quickly evacuate enormous quantities to a pressure of 1×10^{-3} mbar [42].

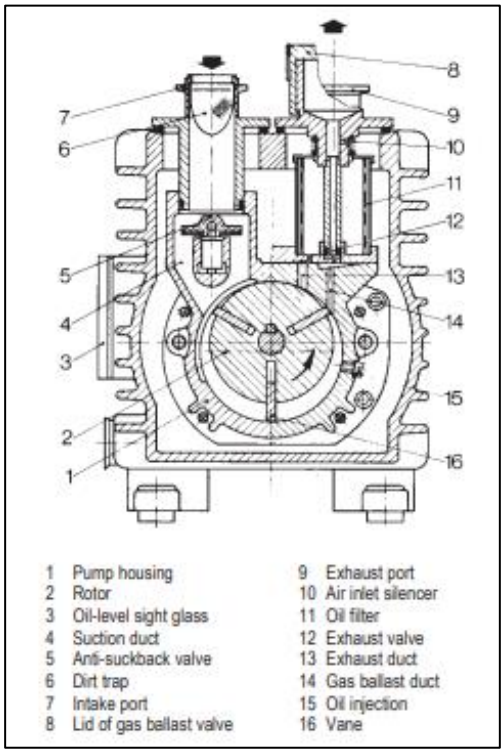

Figure 2. 1: Diagram showing the operation of the rotary vane pump. The illustration shows a cross-section of the pump, and black arrows show the direction of the flow [42].

Turbomolecular Pump

Turbomolecular pumps were created, and are now used, as a result of the desire to benefit from the advantages of oil-free pumping. The turbomolecular pump imparts a preferred direction to a molecular motion similar to the diffusion pump, except in this case the impulse is brought about by impact with a turbine rotor

that is spinning at rates of 20,000 to 30,000 revolutions per minute. The turbomolecular pump is a vertical, axial flow compressor that uses numerous stages or rotor-stator pairs mounted in succession to provide gas molecules direction by ballistic transport (see Fig. 2.2). Gas that has been trapped by the upper stages is passed to the lower stages, where it is incrementally compressed to the fore-vacuum pressure [41].

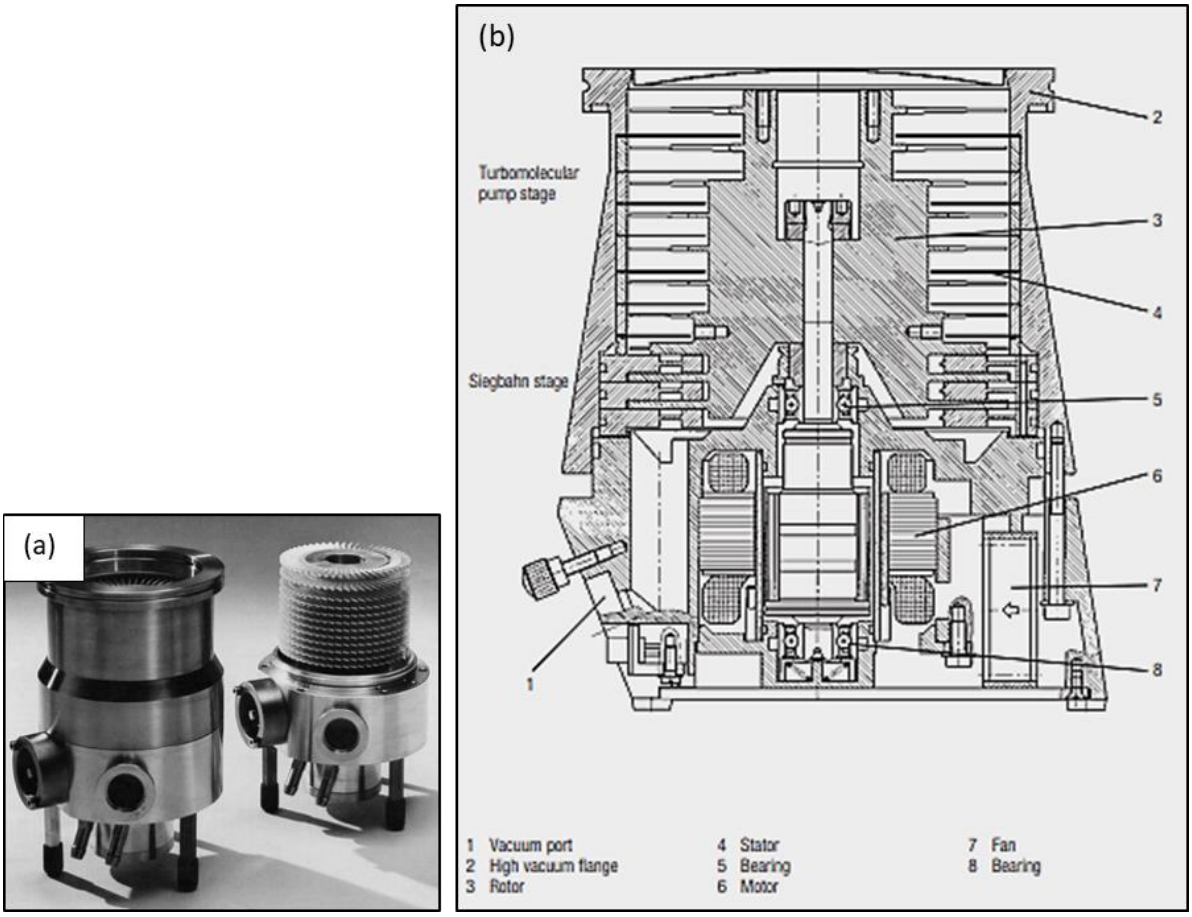

Figure 2. 2: (a) turbomolecular pump (b) Diagram showing the operation of a turbomolecular pump [42].

While the blades spin at speeds of up to 30,000 revolutions per minute, the pump will become frictionally heated as a result of frequent contact with the gaseous atmosphere. Hence, the pumps are only used once the chamber's pressure has been decreased to about 1×10^{-3} mbar. A rotary pump can support the turbomolecular pump to efficiently achieve oil-free pumping. Although turbomolecular pumps are typically the most significant pumps used in growth chambers, other applications that are sensitive to noise, such as electron microscopes, cannot use them because of the rotation of the blades [42].

New generations of pumps, such as the ion pump and Titanium sublimation pump, have been created to address the issues with noise and oil back-streaming. Reactive ions are used in these novel pumps to bond with the chamber's remaining ions and subsequently bond them to the pump's components or the chamber walls.

Ion Pumps

Ion pumps are molecule-trapping devices that store air molecules inside of them and let them out when switched off or heated, respectively (see Fig. 2.3). In order to trap gas atoms, the intense gas ions sputter Ti atoms from the cathode, which then condense throughout the pump chamber, primarily on the cylindrical anode. Ion pumps thus eliminate gas atoms through electrical attraction to the cathodes and chemisorption on the anode surfaces.

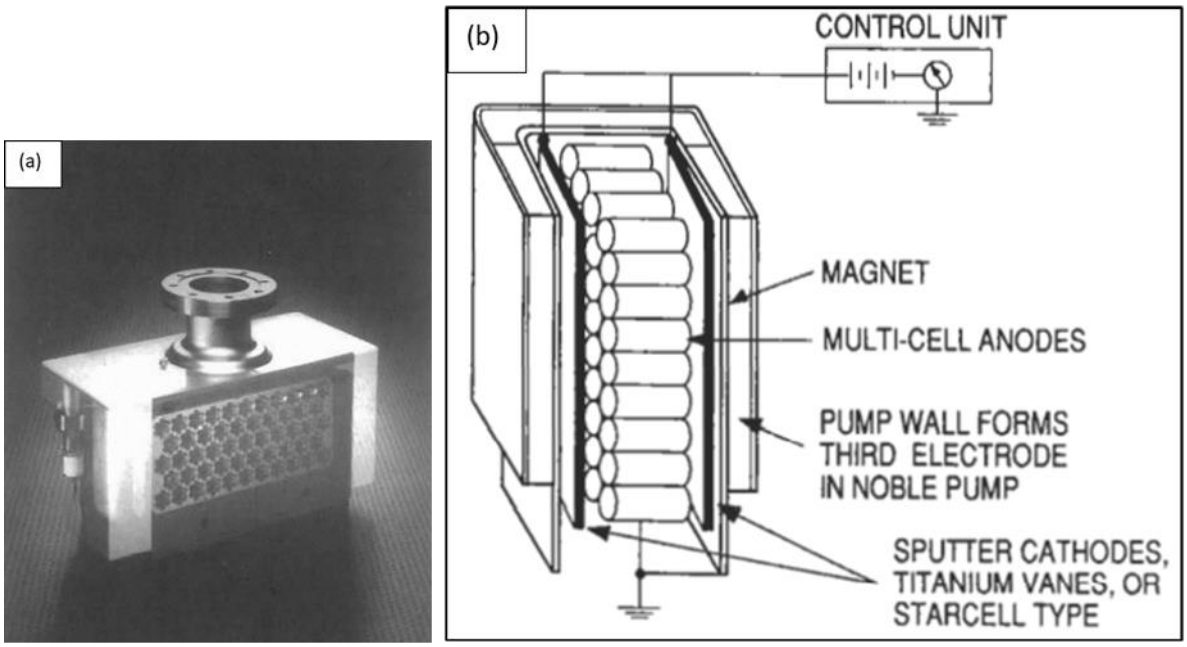

Figure 2. 3: (a) Ion pump; (b) schematic representation of the interior of ion pump [41].

Ion pumps are often turned on after a diffusion pump has decreased the pressure to $<\sim 10^{-3}$Pa because they are only effective at high vacuums. Ion pumps are frequently added directly to the stage or gun chambers of TEM [42].

Titanium Sublimation Pump (TSP)

This is an entrapment pump that helps in maintaining UHV conditions by lowering the pressure from 1×10^{-9} mbar to below 1×10^{-10} mbar. A thin coating is created on the inside surfaces of the chamber by intermittently sublimating Ti atoms, which traps reactive gases like hydrogen, oxygen, and nitrogen (see Fig. 2.4). The TSP can quickly restore the vacuum after gaseous expansion by

efficiently removing gases that pose a greater challenge to the turbomolecular pump. Even though TSPs are a finite source pump, once the Ti source is exhausted, the chamber must be vented and the source must be changed. As a result, the length of the pump cycle is frequently several hours.

Once growth has begun, the TSP should be evaluated for its cycle position and maybe switched off to prevent contamination of the growth by titanium.

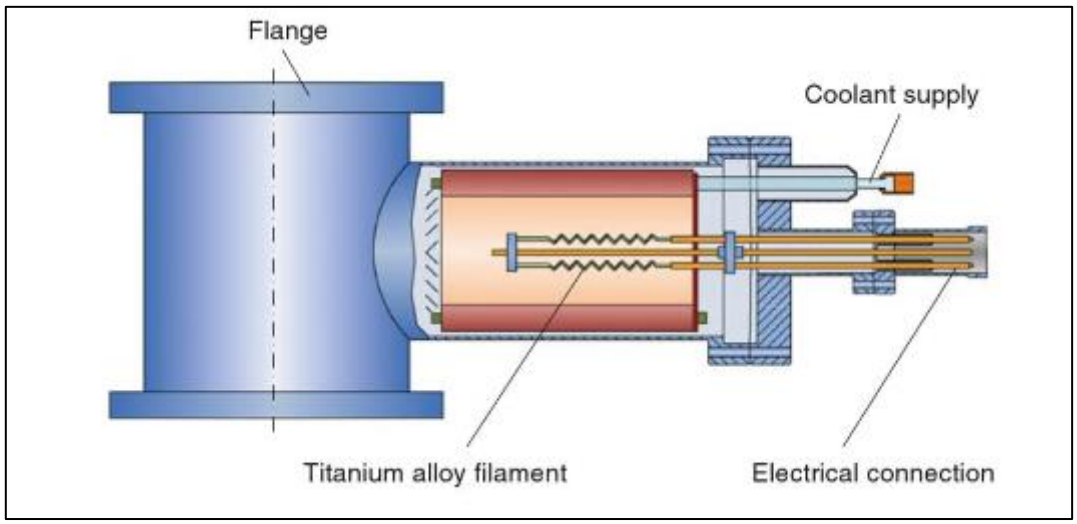

Figure 2. 4: Schematic representation of the interior of TSP [43].

Vacuum Gauges

The two different vacuum gauges, Pirani and ion gauges, are used to measure pressure. The employment of these two instruments is necessary since they both operate at different vacuum levels. Pirani gauges can read pressure in a rough vacuum (1mbar to 1×10^{-3} mbar), whereas ion gauges can only function in high vacuum and above conditions ($<1 \times 10^{-9}$ mbar). As both gauges are calibrated for the same gas species, nitrogen, they are regarded as indirect pressure gauges and are therefore subject to uncertainty.

Pirani gauges measure pressure by detecting heat transfer away from a resistively heated wire. After the temperature has had time to stabilise, a precisely measured current is applied to the wire, and the resistance of the wire is then measured. The quantity of heat dissipated from the wire may be determined since the resistance of the wire is linearly proportional to the temperature. The atmospheric pressure is directly proportional to this value. The low gas density makes it impossible to calculate heat transfer at pressures below those of the high vacuum domain. The pressure is instead determined by ion gauges, which track the flow of ionised molecules. The collision of produced electrons forms ions and the ion current

measures the density of the gas in the system, and hence the pressure. The ion gauge is vulnerable to oxidation and can be damaged at high pressures because of the gathering of ions.

2.1.2 Molecular Beam Epitaxy

Optical, semiconductor and spintronic devices, including solar cells, diodes, storage devices, sensors, transistors, and other integrated circuits, are directly dependent on the growth of metal-oxide thin films. The epitaxial growth is important in the deposition of semiconductor materials for forming good-quality layers [44].

MBE (shown in Fig. 2.5) is a well-established UHV growth technique for producing thin films layer by layer on a heated crystalline substrate. The growth will be better if the layers or deposits have the same crystalline structure as the substrate or a structure with similar symmetry and a lattice parameter difference from the substrates of no more than 10%. The formation of an ordered lattice depends on the effective mobility of adsorbed species on the growing surface, which is activated by the comparatively high substrate temperatures. The beams are often created by the evaporation or sublimation of appropriate materials confined in ultra-pure crucibles. The film stoichiometry, thickness, and doping concentration can be controlled precisely using the MBE technique. The high quality of the produced films and the purity of the grown films is the strength of MBE compared to other deposition techniques [45].

MBE is also used to deposit organic semiconductors with minimised auto doping and auto diffusion. Instead of atoms, in this approach molecules are used in the growth process. The role of MBE in the growth of semiconductor materials and in electronic and photonic devices makes epitaxial growth commercially important. The availability of diagnostic methods in growth or analysis chambers, all coupled under ultra-high vacuum is one of the most notable features of MBE.

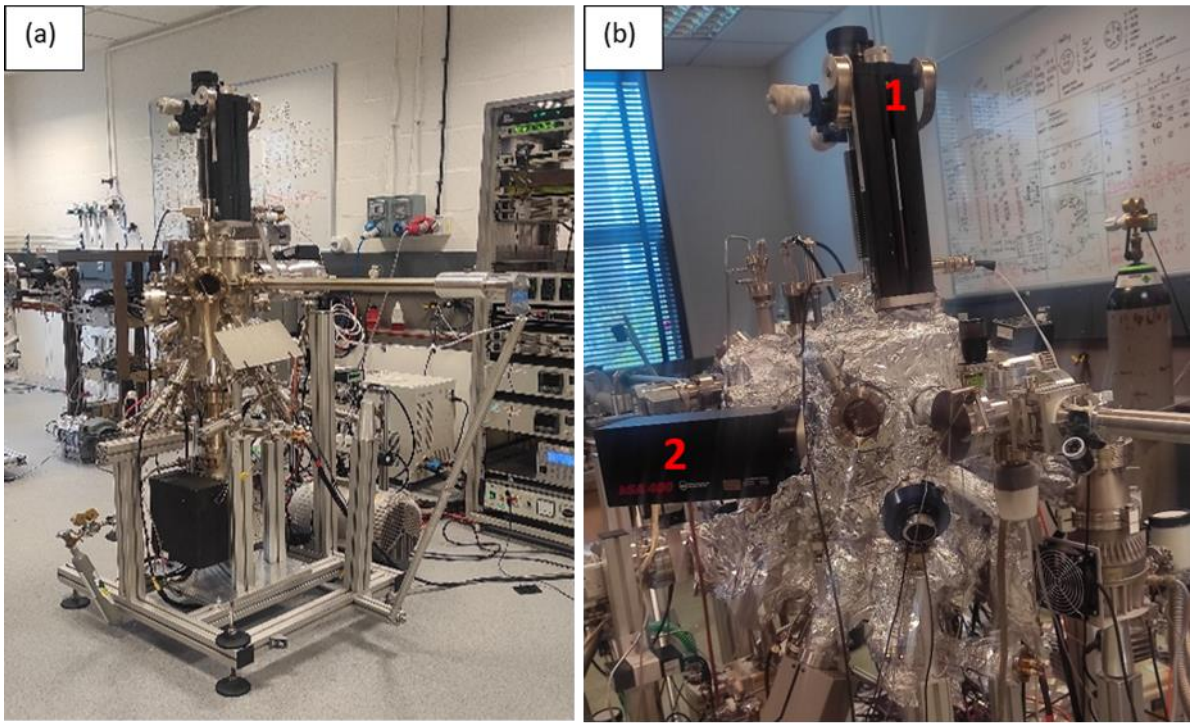

Figure 2. 5: (a) view of the MBE chamber used in the project. (b) Specific inlets are numbered and correspond to the following: 1) stage manipulator 2) RHEED.

A detailed understanding of growth mechanisms is made possible by the application of these approaches, which are occasionally available in-situ (in the growth chamber) and in real-time (during the growth), which in turn explains why MBE procedures can be regulated extremely precisely and with high yields [45].

The three fundamental steps that may be used to explain this ultra-high vacuum-based technology are (i) the creation of atomic/molecular beams, (ii) transportation of the particles to the substrate, and (iii) deposition onto the substrate. The thermal vaporisation of solid elements or compound ingredients or the delivery of gaseous constituents causes the creation of atomic/molecular beams. To obtain a homogeneous composition and thickness of the films, high flux stability during evaporation is necessary. A mean free path for the particles of the beam greater than the separation between source and substrate can maintain the beam direction and density.

Usually, this condition can be met with a total pressure of more than 10^{-4} mbar. However, the development of high-quality thin films requires pressures between 10^{-10} and 10^{-11} mbar, which reduces the incorporation of impurities. After the particle hits the substrate, a number of distinct processes may take place, influencing the early stages of the growth. The atom or molecule can move across the surface until it interacts with other particles to create a cluster, gets captured

at specific places like defects or steps, or can be re-evaporated and deposited at a fixed location.

The process of MBE deposition takes a long time because only one monolayer is deposited every minute. A modest growth rate is necessary in order for the atomic layers to form layer by layer, and also for the atoms to have enough time to diffuse on the surface and enter their lowest energy configuration. These lengthy deposition times are the reason why UHV conditions are necessary to prevent contamination of the film.

The three basic growth modes for a thin film are (i) island growth (also known as Volmer-Weber), (ii) layer-by-layer growth (or Frank-Van der Merwe), and (iii) the layer plus island or Stranski-Krastanov growth. The strength of the bonds between each adatom and the substrate, as well as between the adatoms themselves, affects the growth mechanism. Other factors that affect the growth mechanism include substrate temperature, growth rates, and structure of the substrate.

A stronger link between the adatoms to one another than to the substrate causes island growth, in which the clusters nucleate and create three-dimensional islands. On the other hand, layer-by-layer growth takes place when the deposited species have a strong connection to the substrate, that leads to the production of two-dimensional sheets. These two modes are combined in the layer plus island or Stranski-Krastanov development process. The succeeding atoms begin to form islands after the development of one or more monolayers.

The technology we used (shown in Fig. 2.5 and Fig. 2.6) consists of a main chamber with fourteen ports made of stainless steel and protected by a gate-valve Fast-Entry Load-Lock (FEL) for load transfer between ambient and UHV conditions. A rotary-backed turbomolecular pump is used to pump both the main chamber and the FEL. As a result, the FEL can be independently vented to atmospheric pressure from the main chamber, and the employment of a turbomolecular pump enables quick recovery of the vacuum to sufficient levels prior to opening the gate valve for sample transfer.

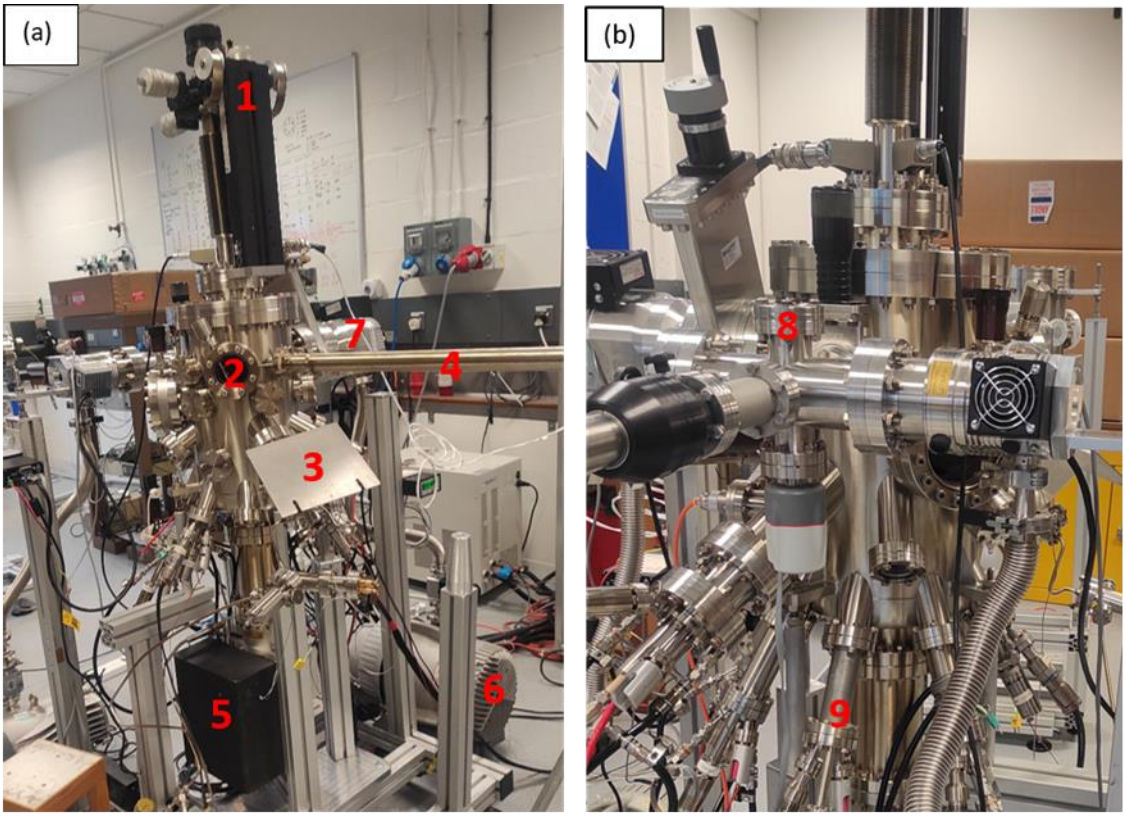

Figure 2. 6: (a) and (b) Photograph of the metal MBE system with specific inlets numbered 1) stage manipulator; 2) metal growth chamber; 3) oxygen plasma; 4) load arm; 5) ion pump; 6) rotary pump; 7) turbomolecular pump; 8) fast-entry load-lock; 9) effusion cells (K-cells).

The main MBE chamber is equipped with three gas inlets that are connected to oxygen, hydrogen, and nitrogen lines and are controlled by two leak valves and one needle valve. A plasma generator that can produce a 100W atomic oxygen plasma and permit molecular oxygen to pass through is attached to the oxygen line. A hydrogen cracker, which can produce atomic hydrogen to prepare substrates for growth, is connected to the hydrogen line. The last gas line is only used for venting and enables nitrogen to be poured into the chamber; it is controlled by a needle valve as opposed to leak valves, which are used to finely regulate the other two lines. The main chamber also has a RHEED system (Fig. 2.5), effusion cells or k-cells (Fig. 2.6), and a Quartz Crystal Microbalance (QCM). RHEED and QCM are used for in-situ monitoring of the growth. Additionally, a TSP (shown in Fig. 2.4) that runs for 20 minutes every four hours is installed in the main chamber. This aids in lowering the partial pressure of the gases (oxygen, hydrogen, and nitrogen) that are delivered to the system to enable speedy restoration of UHV conditions following a growth or chamber venting.

Sample manipulator and sample holder

One of the essential elements of the MBE system is the sample manipulator. It is a Vacgen HPT-WX manipulator in this instance, with modules for X, Y, and Z motion, a module for X, Y rotation, and a heating sample stage (shown in Fig. 2.7). The sample stage is suitable for use in UHV and O_2 environments because it is comprised of stainless steel and Inconel. The sample is fixed using two Inconel clamps so that it can be placed face down for growth. It is possible to reach temperatures of up to 1100°C during this heating stage. The stage contains a U-shaped hole in one of the sides to allow grazing angles for the RHEED gun's electrons to hit the substrate.

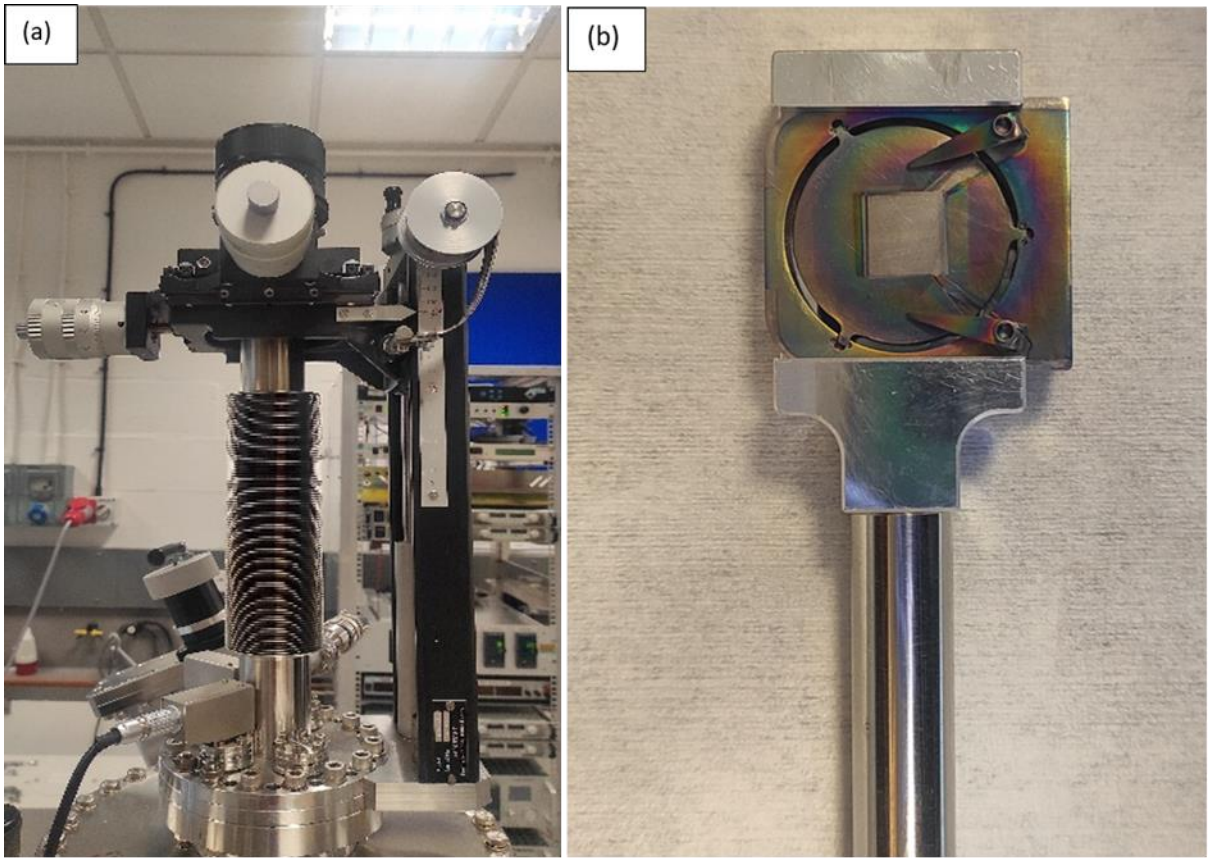

Figure 2. 7: Photograph of (a) Vacgen HPT-WX manipulator, (b) heating stage and sample holder.

Film growth

The growth process is carried out in a UHV environment that is produced by the continuous pumping of the turbo pump. The sample holder with a substrate is attached to the sample manipulator (Vacgen HPT-WX) which can be rotated during growth (shown in Fig. 2.7). The MBE chamber that we employ to deposit solid materials uses Knudsen-type effusion cells (K-cells), positioned at the

bottom of a UHV chamber and oriented towards the centre of the chamber where a sample holder with a substrate is located (shown in Fig. 2.6). These cells are made up of a crucible and are heated until the elements in each cell reach the sublimation point. Following that, the shutters that can be operated from outside of the chamber are opened, allowing the physical vapour from each K-cell to diffuse through the chamber and deposit itself on the substrate. The substrate's temperature, atomic structure, and flux ratios of the various components reaching the substrate will all affect the final composition and stoichiometry of the film. Combining a power source and a thermostat allows for precise control of the source temperature and constant flux throughout the deposition. Further, the grown films were in-situ annealed in the MBE chamber using molecular oxygen with an oxygen partial pressure of 5×10^{-6} mbar.

A QCM is lowered into the deposition position within the chamber to measure the rate of deposition. Calculating the rate of deposition by keeping track of the quartz crystal's resonant frequency is possible when the parameters of the material being deposited, including its density and elastic moduli, are known. The properties of the QCM, such as the mass, dimensions, elastic moduli, and density, all alter as the material is deposited on it. As a result, the crystal's resonance frequency is also altered. An accurate measurement of the deposition rate can be obtained by calculating the amount of material and time needed to complete the shift. Because the frequency of the crystal is temperature dependent, it is crucial to read the change after the crystal has had time to readjust to its surroundings.

2.2 Characterization Techniques

This section will focus on both In-situ and Ex-situ structural characterisation techniques used for this study.

2.2.1 Reflection High-Energy Electron Diffraction

RHEED is a characterisation method that can be used to keep track of the structure and composition of epitaxial films as they grow in-situ. Due to the sensitivity of diffraction to adsorbed contaminants and the requirement to prevent electron-beam scattering by gas molecules, an ultrahigh vacuum environment is essential for this approach. In RHEED, electrons under small angle hit the specimen surface and their diffraction is then captured on a fluorescence screen. In contrast to X-ray diffraction (XRD), which assesses the bulk of the material, in RHEED the electrons will only penetrate a few Å into a sample. An electron gun, a sample with a spotless surface, and a fluorescence screen are the three basic elements of a RHEED experiment. A schematic representation of the RHEED system used in this work is shown in Figure. 2.8. In general, the energy of the electron beam can be adjusted to be between 8 keV and 30 keV in RHEED

experiments, but in our case, the electron beam is set to an energy value of 15 keV and it typically strikes the sample at an incidence angle of between 1° and 4°.

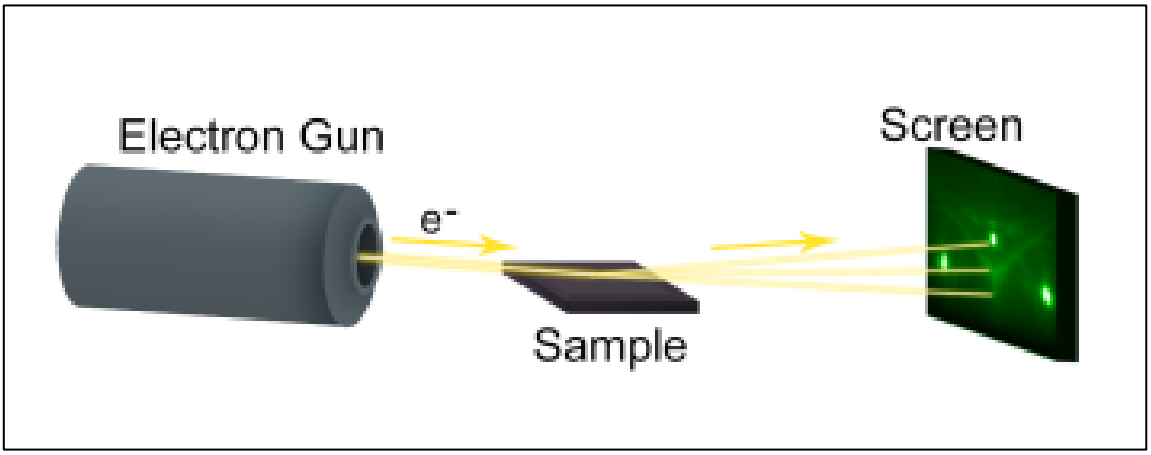

Figure 2. 8: Experimental arrangement of the RHEED technique [46].

According to Bragg's rule, electrons coherently scatter and generate interference patterns that can be seen in a fluorescent screen. Understanding reciprocal space is necessary to describe how a diffraction pattern develops from the scattering of numerous electrons in RHEED. The real lattice is how atoms are arranged in a crystal. A different way to describe the crystal structure using planes that have a reciprocal relation to the actual lattice geometry is the reciprocal lattice. As a result, smaller dimensions in reciprocal space will be larger in real space, and vice versa. The spacing of the features in the diffraction pattern is consistent with reciprocal space. The reciprocal surface lattice vector can be given as

$$r^* = m_1\mathbf{a}^* + m_2\mathbf{b}^* \qquad (2.1)$$

where m_1 and m_2 are integer scaling factors and $\mathbf{a}^*$ and $\mathbf{b}^*$ are the reciprocal basis vectors. The Miller indices (h k l) are employed to provide plane orientations in reciprocal space. The (h, k) indices are used to represent the surface geometry in two dimensions. A surface's continuous third dimension can be represented as lattice rods in reciprocal space. Since the locus of all possible final wave vectors for elastically scattered electrons is a sphere, Bragg's law can be applied to create a continuous sphere of possible diffraction angles. This sphere is known as the Ewald sphere (shown in Fig. 2.9) and its radius is dependent on the incident electron beam's energy. High electron energies in RHEED result in a massive Ewald sphere [41]. The diffraction pattern that will appear on the fluorescence screen is reproduced at the point where this sphere intersects the reciprocal lattice.

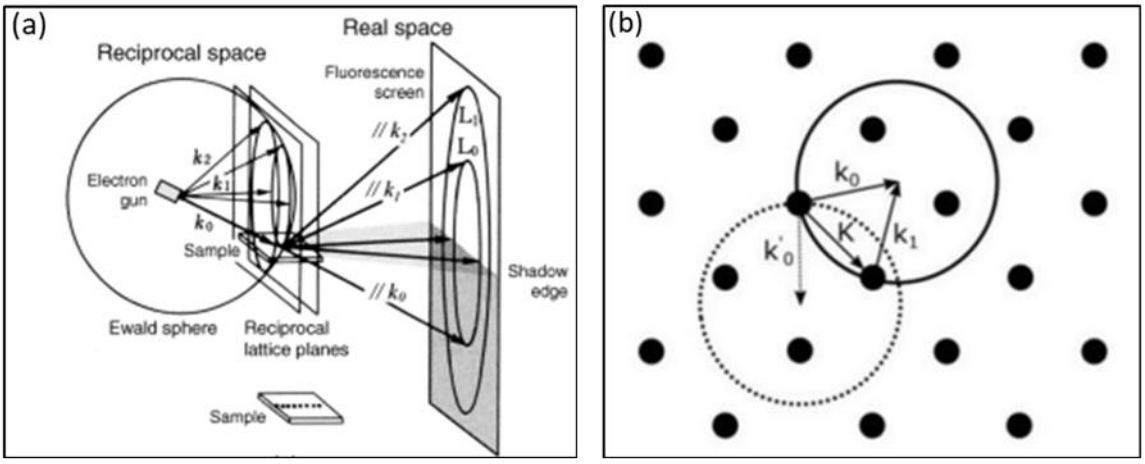

Figure 2. 9: a) Ewald construction for a 2D plane in reciprocal space and as viewed on the RHEED fluorescence screen, (b) 2D representation of the Ewald sphere [46].

The RHEED pattern differs significantly for various surfaces, which demonstrates the surface sensitivity of RHEED [46]. Both spotted and streaked patterns can be seen during MBE film growth (shown in Fig. 2.10).

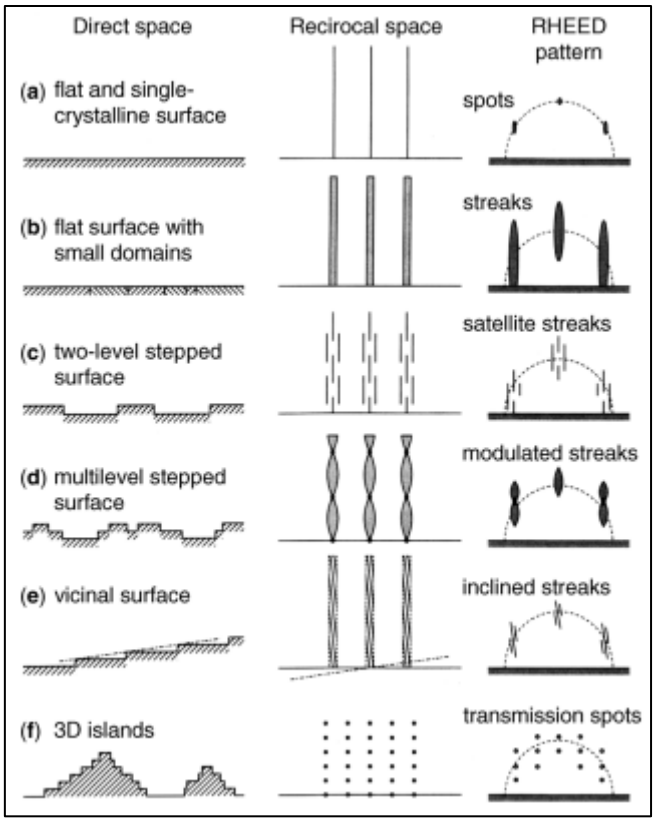

Figure 2. 10**:** Different RHEED patterns corresponding to different surfaces [46].

Due to lattice imperfections and thermal vibrations, the reciprocal lattice rods have a finite width, and the incident electron energy spread also causes the Ewald

sphere to have a finite width. As a result, the Ewald sphere and rods connect along some of their height, producing a streaked rather than spotty diffraction pattern. Spots are a result of smooth layered film growth, whereas streaks are caused by three-dimensional volume diffraction at islands or surface asperities.

2.2.2 Electron Microscopy

Electron microscopy is a method that allows analysis of the atomic structure and chemical composition of materials on sub nm scale. The limited image resolution in light microscopes, which is imposed by the wavelength of visible light, led to the development of electron microscopes. The idea that the electron possessed wave-like properties and had a wavelength far smaller than visible light was initially put forth by Louis de Broglie in 1925. Then, in 1927, two research teams including Davisson and Germer and Thomson and Reid separately conducted their well-known electron-diffraction experiments, proving the electrons' wave-like character [47]. Since the wavelength of highly energetic electrons can be up to 10^5 times shorter than the wavelength of photons, electron microscopes have a significant resolution advantage over traditional optical microscopes. The well-known de Broglie formula provides the wavelength of the accelerated electrons as:

$$\lambda = \frac{h}{p} \tag{2.2}$$

where p is the particle's momentum and h is the Planck constant [48].

A relativistic analysis of the momentum is necessary when accelerating electrons through a high potential, typically 100-300 keV, as this results in the electron travelling at a speed greater than half that of light. The de Broglie equation can be revised to consider these relativistic effects using V, the electron beam's perceived accelerating potential.

$$\lambda = \frac{h}{\sqrt{2m_e eV\left(1+\frac{eV}{2m_e c^2}\right)}} \tag{2.3}$$

Here, an electron's mass and charge are shown by the letters m_e and e, respectively, with c standing for the speed of light in a vacuum. Higher accelerating potentials should be applied to shorten the wavelength and hence improve theoretical resolution. Additionally, this enables penetration through thicker samples, which is significant because transmission electron microscopy needs samples to be less than 100 nm thick in order for them to be electron transparent. However, a higher accelerating potential makes the sample more sensitive to beam damage. In some situations, the electron beam can even destroy the sample.

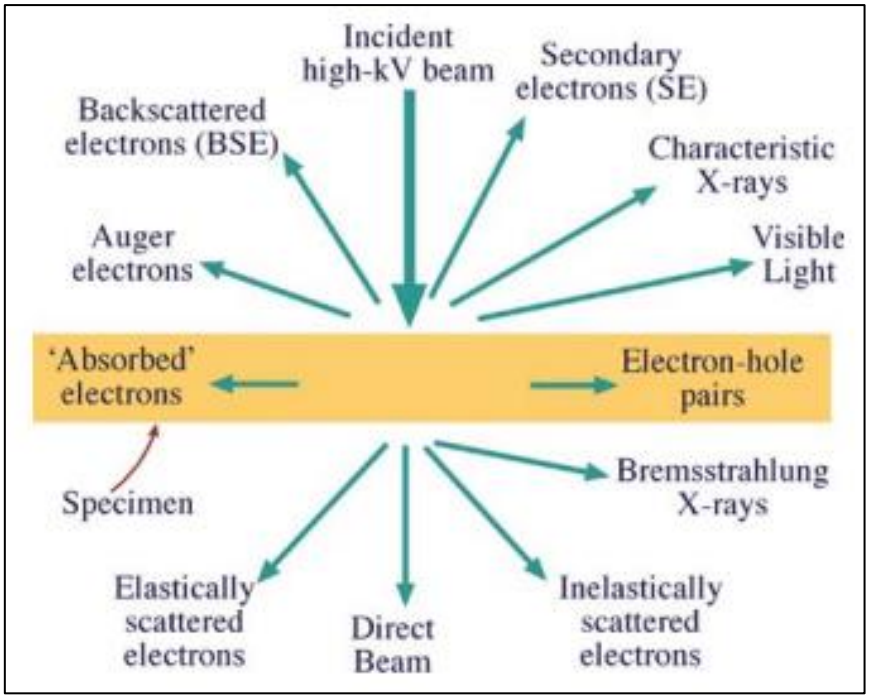

Figure 2. 11: The different signals that emit due to the interaction of electrons with the incident beam [49].

In an electron microscope, the specimen and incident electrons interact to produce a variety of exit signals that are captured and analysed (shown in Fig. 2.11). The two primary types of electron microscopes are the SEM and the TEM. TEM uses the direct beam and the transmitted elastically scattered electrons to generate images with the use of electromagnetic lenses, whereas the secondary and backscattered electrons are the most significant signals for an SEM.

Electron Lenses

Electromagnetic lenses are one of the most crucial components of any electron microscope. An electron gun, a combination of electromagnetic lenses, apertures, a sample holder, and an image viewing or recording system all together form an electron microscope. A charge-coupled device (CCD) camera or a fluorescent viewing screen detects the high-energy electrons that are generated by the gun after they have been deflected and focussed inside the microscope column. The illumination system refers to the set of lenses that is situated between the electron gun and the specimen. These lenses collect the electrons leaving the gun and direct a parallel beam of them at the specimen. An additional intricate system of lenses including objective, intermediate, and projector lenses are employed to magnify and record either a picture or a diffraction pattern after the electrons have interacted with the object. The electron beam, the images, and the diffraction

patterns are magnified and focused using electron lenses throughout almost every operation on the EM.

Analysis of diffraction patterns is important in TEM studies since it can reveal more information about the crystal structure than a TEM image does. Electrons scattered across a specimen cause both constructive and destructive interference, which results in diffraction patterns. As shown in Figure. 2.12, the diffraction pattern of the crystalline samples will be an array of sharp spots and for the amorphous material, it will be diffused rings.

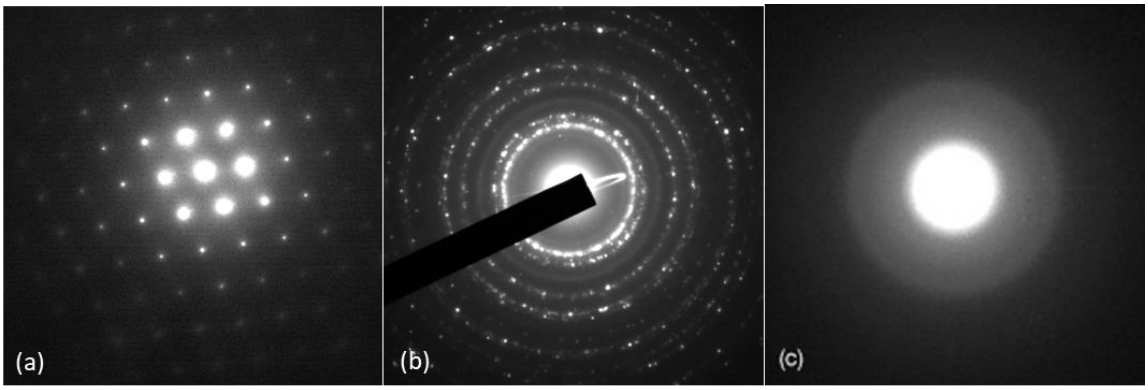

Figure 2. 12: Electron diffraction patterns for (a) single crystalline, (b) polycrystalline (taken from my experimental data) (c) amorphous material [50].

The electron lenses in the TEM are the equivalent of the glass lenses in a visible light microscope (VLM). The lenses in a TEM operate the instrument's fundamental functions, just like in a VLM. A lens in a visible light microscope will deflect light because of the light path-shifting refractive index. Mirroring this method, transmission electron microscopy uses magnetic fields that are generated to control the electron beam using the Lorentz force. The strength of the electromagnetic lens can be altered by varying the current flowing through the Cu-coil in the lens [49].

Electromagnetic lenses are significantly more defective than optical lenses, even though the magnetic field inside of them offers a controlling mechanism for altering the paths of the electrons. The difficulty arises from the fact that it is quite challenging to produce a magnetic field that operates uniformly on every electron. The most critical factors to consider in order to obtain even better resolutions are astigmatism, chromatic aberrations, and spherical aberrations.

Spherical aberration is the electromagnetic lens inability to behave uniformly towards both off-axis and paraxial electrons. In other words, electrons that are approaching the optical axis at a low angle would be focused differently than

electrons that are approaching it at a higher angle. As a result, a point object will appear as a disc with a finite size, which restricts the resolution of a microscope.

Chromatic aberration is influenced by the electrons "colour," which can be defined as their frequency, wavelength, or energy. It results from a difference in the electrons wavelength in the microscope. The energy distribution of the electrons coming out of the electron gun is the cause of this difference. Instead of the original (source) point, the electrons with reduced energy will form a fuzzy disc on the imaging plane due to increased deflection. By using better electron guns with a smaller energy spread and a monochromator, one might reduce the aberration brought on by the electron source. Better electron guns in modern microscopes (based on cold field emission) can generate electron beams with an energy spread of about 0.3 eV.

Another aberration that reduces the spatial resolution of the microscope is astigmatism. That happens when the electrons detect an irregular magnetic field revolving around the central axis of the microscope. This lowers the resolution of the resulting image. The lenses are one of the main causes of astigmatism, although contamination can also result in charge accumulation on the apertures. The stigmator coils can be used to fix this flaw by producing a compensatory magnetic field that gives the beam a controllable 2-dimensional distortion.

2.2.2.1 Transmission Electron Microscopy

TEM is a high-resolution imaging technique in which an image is produced by a stream of electrons (from the electron gun) passing through a thin sample. Figure 2.13 gives a schematic representation of TEM. The sample composition, crystallinity, and thickness/density all have an impact on the electron beam. The scattering and absorption of electrons in thicker specimen sections and from heavier element atoms define contrast in the image at low magnifications. When the magnification is high, the interference of electrons that were scattered by the specimen and the wave nature of the electrons dominate the image contrast. A set of electromagnetic lenses significantly magnifies these transmitted electron signals. The use of beam energies between 100,000 and 400,000 eV makes TEM a very demanding piece of machinery. TEM even provides vital information about the internal structure of the sample, including data on crystal structure, morphology, and stress states. SAED, HRTEM, Bright field TEM (BF-TEM), and Dark field TEM (DF-TEM) are the four fundamental TEM operations (see Fig. 2.14) [49].

There are four basic lens systems and three major apertures (as shown in Fig. 2.13) in a TEM. The illumination system or condenser lenses, which are the first lens, collect and focus the electrons emitted from the electron source. The

condenser aperture is used to form a collimated electron beam, which helps to reduce the final image's spherical aberration. Since this system is unaffected by the imaging mode, all four modes of operation use the same components. The objective lens comes next; which is a very powerful lens that is frequently regarded as the most crucial lens in a microscope. It creates the images and diffraction patterns that the other lenses magnify. Of all the lenses in the microscope, the objective lens has the widest angle of incident beam. When the intermediate lens is focused on the back focal plane of the objective lens, diffraction patterns can be observed in a TEM. A selected area aperture can be inserted in the first intermediate image plane to specify the region from which the diffraction pattern is extracted. Such images are called SAED pattern.

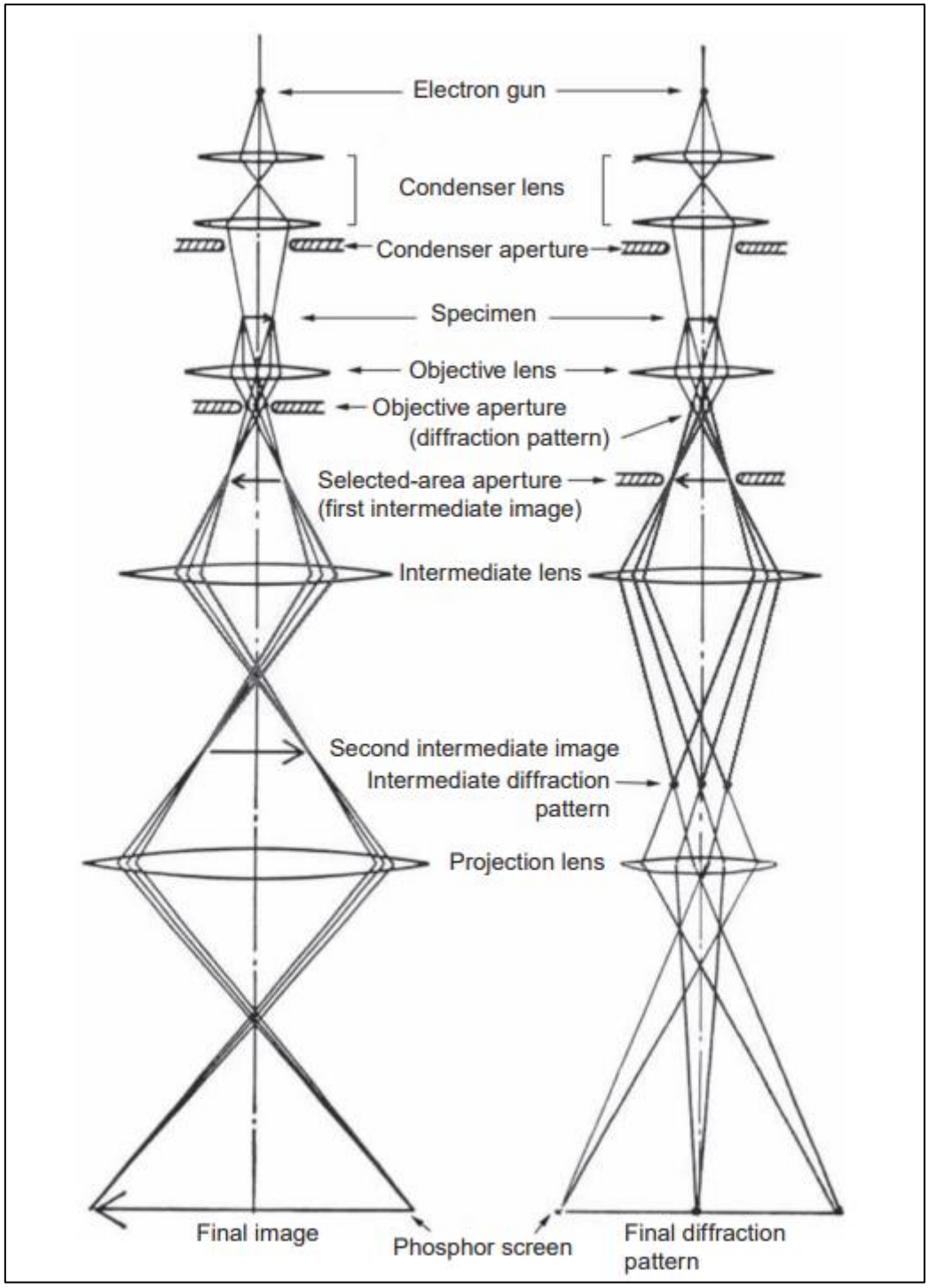

Figure 2. 13: Schematic view of imaging (left) and diffraction (right) modes in TEM [51].

Setting the objective aperture differently distinguishes the two real-space imaging modes, BF-TEM and DF-TEM (shown in Fig. 2.14). The objective aperture, which is positioned in the back focal plane of the objective lens, is used by both BF-TEM and DF-TEM. The objective aperture at the back focal plane, which isolates the unscattered electrons, is used in BF-TEM to enable the direct beam

while blocking the diffracted beam. In this mode, the film can be seen more clearly in the image because the substrate material composition scatters the electron beam differently from the film, creating a contrast between the two. Another diffraction contrast imaging technique that enables the formation of images from diffracted beams is DF-TEM. In this mode, the regions where the electrons scatter at the angle allowed by the chosen Bragg condition are brighter in the resulting image. Due to the fact that the contrast and brightness will be decreased in areas that do not meet the isolated Bragg condition, this mode is helpful for differentiating between phases and grains within the sample. The objective aperture is removed in the third mode, HRTEM, allowing the entire transmitted diffraction pattern to pass from the back focal plane (Fig. 2.14) [49].

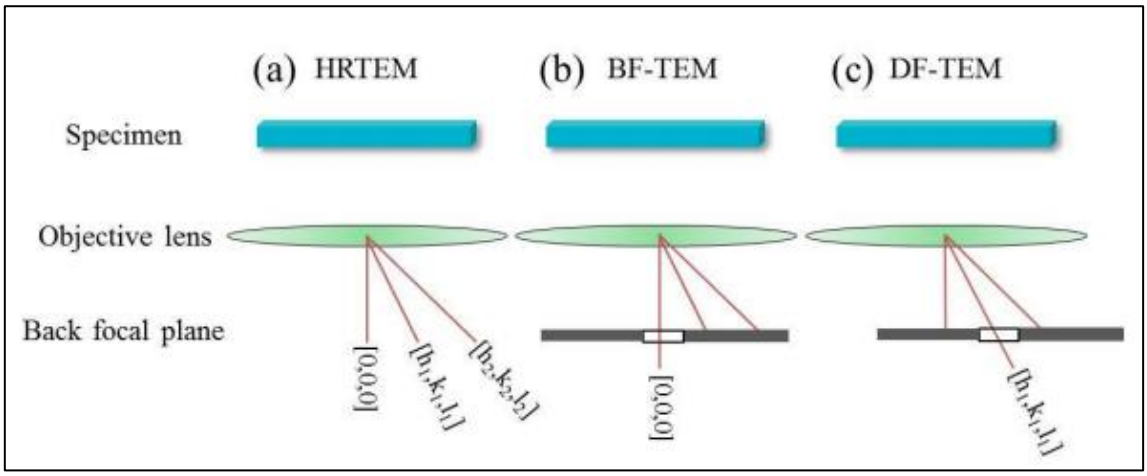

Figure 2. 14: Schematic view of (a)HRTEM, (b) BF-TEM, and (c) DF-TEM [52].

2.2.2.2 Scanning Electron Microscopy

A focused beam of high-energy electrons is utilised by the SEM to produce a range of signals at the surface of solid specimens. In addition to the sample's exterior morphology (texture), SEM/EDS also provide information about the sample's chemical composition, crystalline structure and orientation of its constituent materials, from the signals resulting from electron-sample interactions. An image is created by combining the position of the electron beam with the strength of the signal being detected while it is being scanned in a raster scan pattern. Most often, a portion of the sample surface is chosen for data collection, and a 2-dimensional picture is created to show the spatial variations in these attributes. Conventional SEM methods can be used to image areas with widths of roughly 1 cm to 5 microns in a scanning mode (magnification ranging from 20X to approximately 30,000X, spatial resolution of 50 to 100 nm). The SEM is also able to analyse specific point locations on the sample; this method is particularly helpful in detecting chemical compositions (using EDS), crystalline

structure, and crystal orientations (using diffracted backscattered electrons (EBSD)) in a qualitative or semi-quantitative manner.

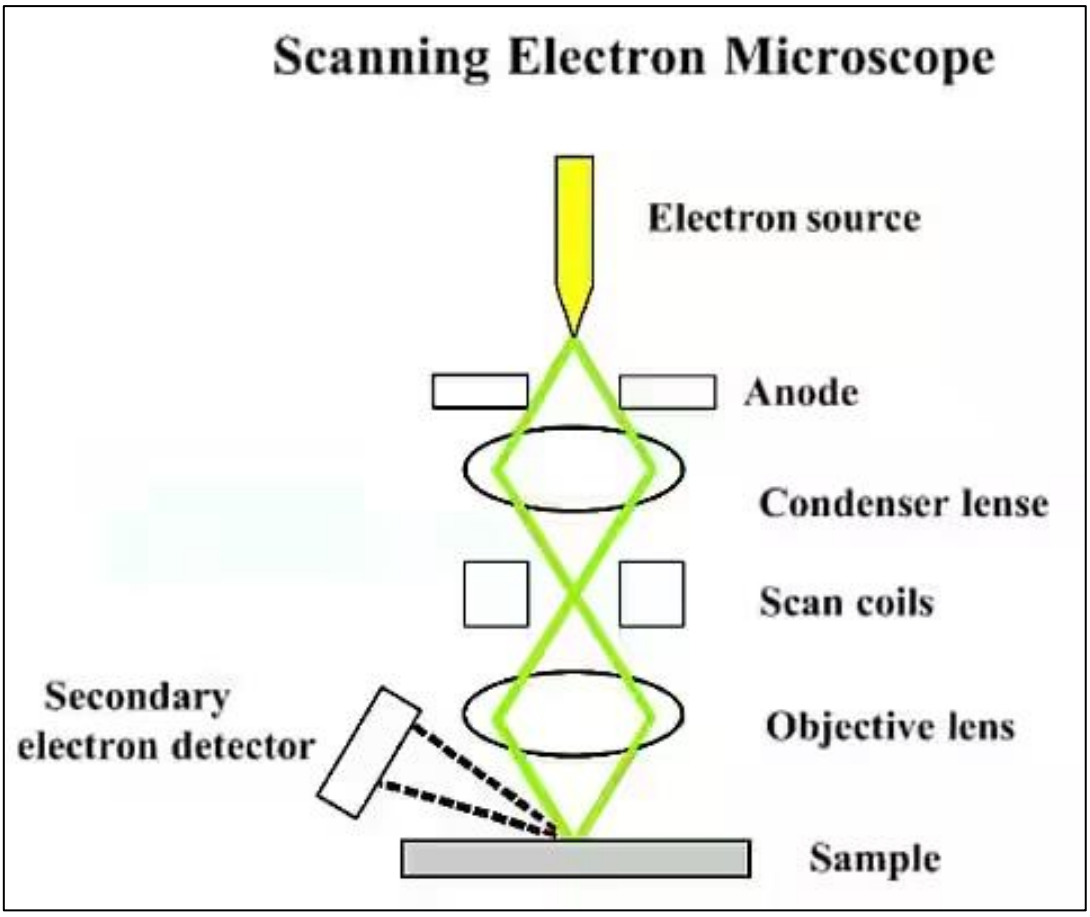

Figure 2. 15: Basic components of an SEM [53].

As shown in Figure. 2.15, a source (electron gun), a set of lenses (objective) that act to control the beam diameter and focus it on the specimen, a set of apertures (micron-scale holes in metal film) that the beam passes through and that affect the beam's characteristics, controls for the specimen's position (x, y, z-height), orientation (tilt, rotation), and an area of beam/specimen interaction, are considered to be the essential components of all SEM and all of the above are maintained at high vacuum levels (the value of the upper column being greater than the specimen chamber). A variety of detectors such as lower electron detector (LED), upper electron detector (UED), upper secondary detector (USD), backscattered electron detector (BED), and EDS are positioned all around the sample chamber to investigate the ways the electron beam can interact with the sample surface (Fig. 2.16).

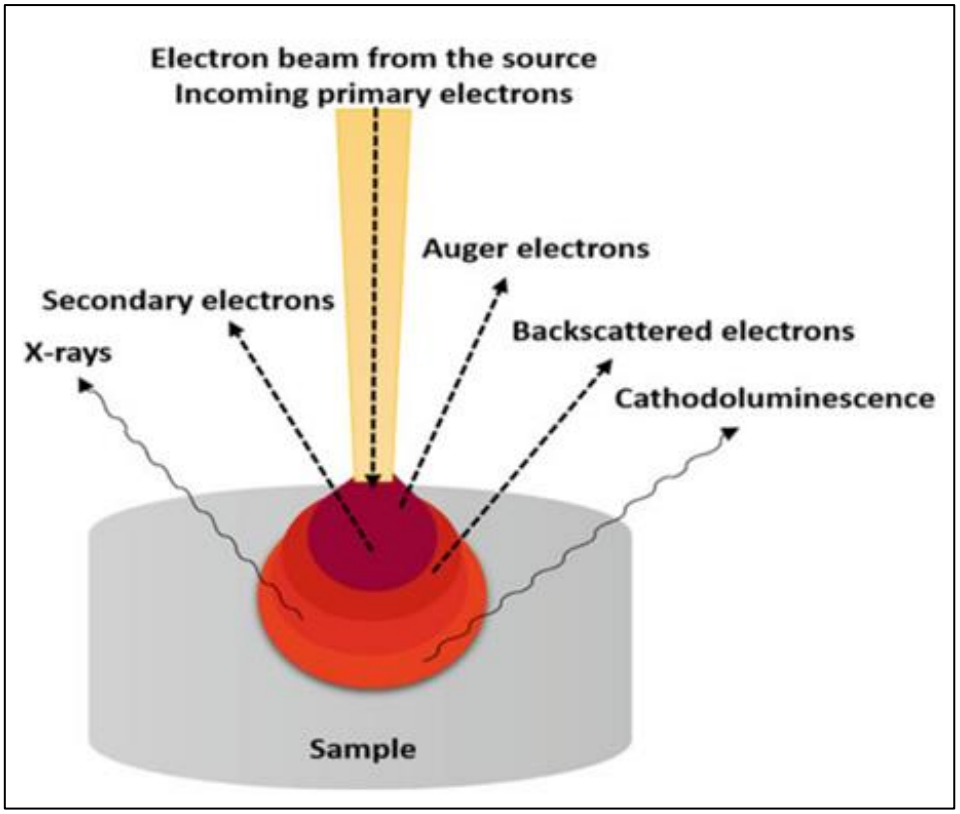

Figure 2. 16: Diagrammatic representation of the signals emitted due to the interaction between the electron beam and specimen [54].

The coulomb (electric charge) field of the specimen nucleus and electrons might interact with the electron beam. Numerous signal types, such as secondary electrons (used to create SEM images), backscattered electrons (BSE), EBSD, photons (characteristic x-rays used for elemental analysis and continuum x-rays), visible light (cathodoluminescence-CL), and heat are produced as a result of these interactions. Both secondary electrons and backscattered electrons can be used to image samples, with secondary electrons being most useful for displaying the morphology and topography of samples and backscattered electrons being most useful for highlighting compositional contrasts in multiphase samples (i.e. for rapid phase discrimination). Inelastic collisions between incident electrons and electrons in certain atomic shells in the sample result in the emission of x-rays. The accelerated electrons produce x-rays with a defined wavelength as they transit back to lower energy states. As a result, each element in a material that the electron beam "excites" emits distinctive x-rays. SEM analysis is regarded as "non-destructive" since the volume of the sample is not lost due to the x-rays produced by electron interactions, allowing for repeated investigation of the same materials [55].

2.2.3 Energy-Dispersive X-Ray Spectroscopy

A sensitive x-ray detector and a software (AZtec) to gather and analyse energy spectra makes an EDS system. An EDS detector (shown in Fig. 2.17 a) is used to separate the distinctive x-rays (produced by the interaction of an electron beam with a sample target) of various elements into an energy spectrum. EDS system software (AZtec) is then used to analyse the energy spectrum in order to calculate the abundance of particular elements. EDS may be used to build element composition maps across a much larger raster region and to determine the chemical composition of materials down to a spot size of a few microns.

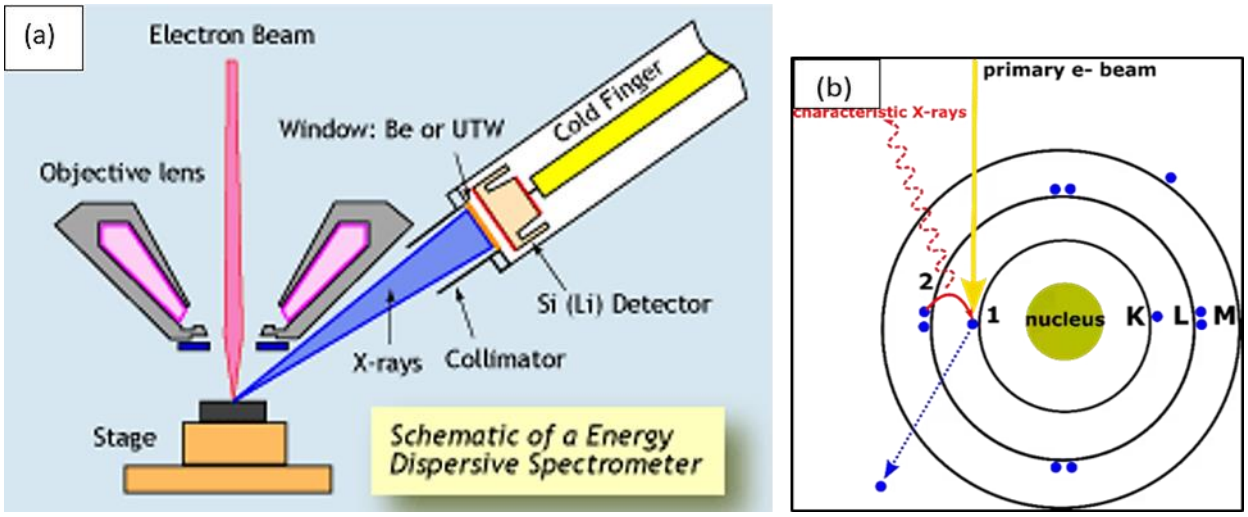

Figure 2. 17: (a)Schematic representation of the Energy Dispersive Spectrometer [56], (b) two-step process of EDS [57].

The EDS detector is built on a semiconductor component, often a silicon crystal. A typical EDS detector is composed of several components such as a collimator, to ensures that only x-rays will be caught in a detector; a window that separates the detector crystal from the chamber of the microscope under a high vacuum; a semiconductor crystal to absorbs the energy of incoming x-rays and electronics for detecting the charge the detector recorded, converting it to a voltage pulse, and sending it to the pulse processor. The pulse processor receives a charge signal created when a high bias voltage is placed across the crystal, which causes electrons and holes to migrate to electrodes on opposing sides of the crystal [58].

When an atom's inner shell is struck by an electron beam for EDS analysis (as shown in Fig. 2.17 b), the electron is knocked out of the shell and leaves a positively charged electron hole. In order to replace the void left by the displaced electron, it attracts another electron from an outside shell. An x-ray can be produced as a result of the energy difference that occurs as the electron transitions from the outer, higher-energy shell to the inner, lower-energy shell of the atom.

This transition determines the energy of the x-ray. In this manner, each element present in a sample can be identified using x-rays [56].

2.2.4 Atomic Force Microscopy (AFM)

AFM is a surface analysis method to scan the the topographic details of samples at the nanometer range. As shown in Figure. 2.18 (a) the microscope has a tip that is attached to a cantilever and a laser beam that is reflected onto a position-sensitive detector from the rear of the cantilever. The position of the cantilever and the reflected laser beam change in response to the atomic forces acting between the probe and the sample, and the detector records the resulting position changes [58].

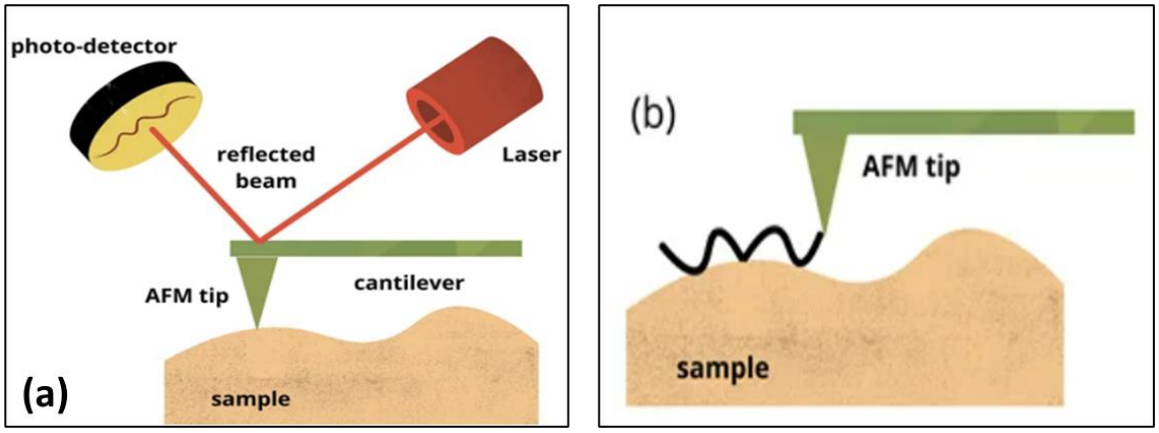

Figure 2. 18: (a) Schematic representation of an AFM, (b) illustration of the tapping mode [59].

In a typical AFM, two measuring methods are often used. The simplest is the contact mode, in which the sample surface is directly touched by the tip to determine the topography. By altering its position, an electronic feedback loop maintains the tip's continuous deflection. Nevertheless, there are a few issues with this mode. Both the tip and the sample surface can easily be damaged since the tip presses down on the sample. On the other hand, as shown in the Figure. 2.18 (b) in the tapping mode (used in this project), the sample's topography is determined by tapping the surface repeatedly at the resonance frequency of an oscillating cantilever. The contact forces will cause the tip's vibration amplitude to diminish as it gets closer to the sample's surface. The tapping mode is less damaging in this instance because the feedback loop maintains the amplitude of the vibrating cantilever and prevents the tip from being in continual mechanical contact with the surface.

2.3 Sample preparation

The techniques used for the preparation of samples for both TEM and SEM/EDS analysis will be discussed in the following section.

2.3.1 Preparation of cross section specimens for TEM - Manual polishing

The first step in preparing a sample for TEM is to cut the sample so that a face of the sample is exposed in cross section. The imaging and analysis of thin film surfaces depend on this. A spinning diamond-coated saw (shown in Fig. 2.19 a) is used to cut the sample into two 2.5 × 1 mm wide strips with the short edge parallel to the chosen viewing direction. The sample is mounted on a glass slide using Crystal Bond from Agar Scientific. As shown in Fig. 2.19 (c) two slightly longer Silicon (Si) strips, 3 × 1 mm in size, are also cut and employed as the sample's supports in addition to these. After being sliced, the material goes through a two-stage chemical cleaning procedure that involves 2-3 minutes of acetone immersion followed by isopropanol immersion, both for the same amount of time and in a sonicator. The sample cuts and Si supports are used to create a multi-layer structure after cleaning. The two cuts of the sample are sandwiched (shown in Fig. 2.19 c) between the Si supports in this structure and are bonded film-on-film. The components are all glued together using a little amount of Gatan G1 epoxy resin in a 1:10 ratio (mix 1-part hardener to 10 parts resin). The glued sample is then placed on a hotplate (set to 135°C) to allow the epoxy resin to solidify. The sample is attached to a glass slide using the Crystal Bond once the epoxy has dried, at which point manual polishing can start. Fig. 2.19 (b) depicts the schematic representation of the composition of the structure. The first stage of polishing is done by polishing the back side slowly (2-3 minutes each pad) with 15, 9, 3, and then with1µm diamond polishing pads. Upon removal from the Crystal Bond, the sample is cleaned using the same procedure (acetone followed by isopropanol) mentioned earlier.

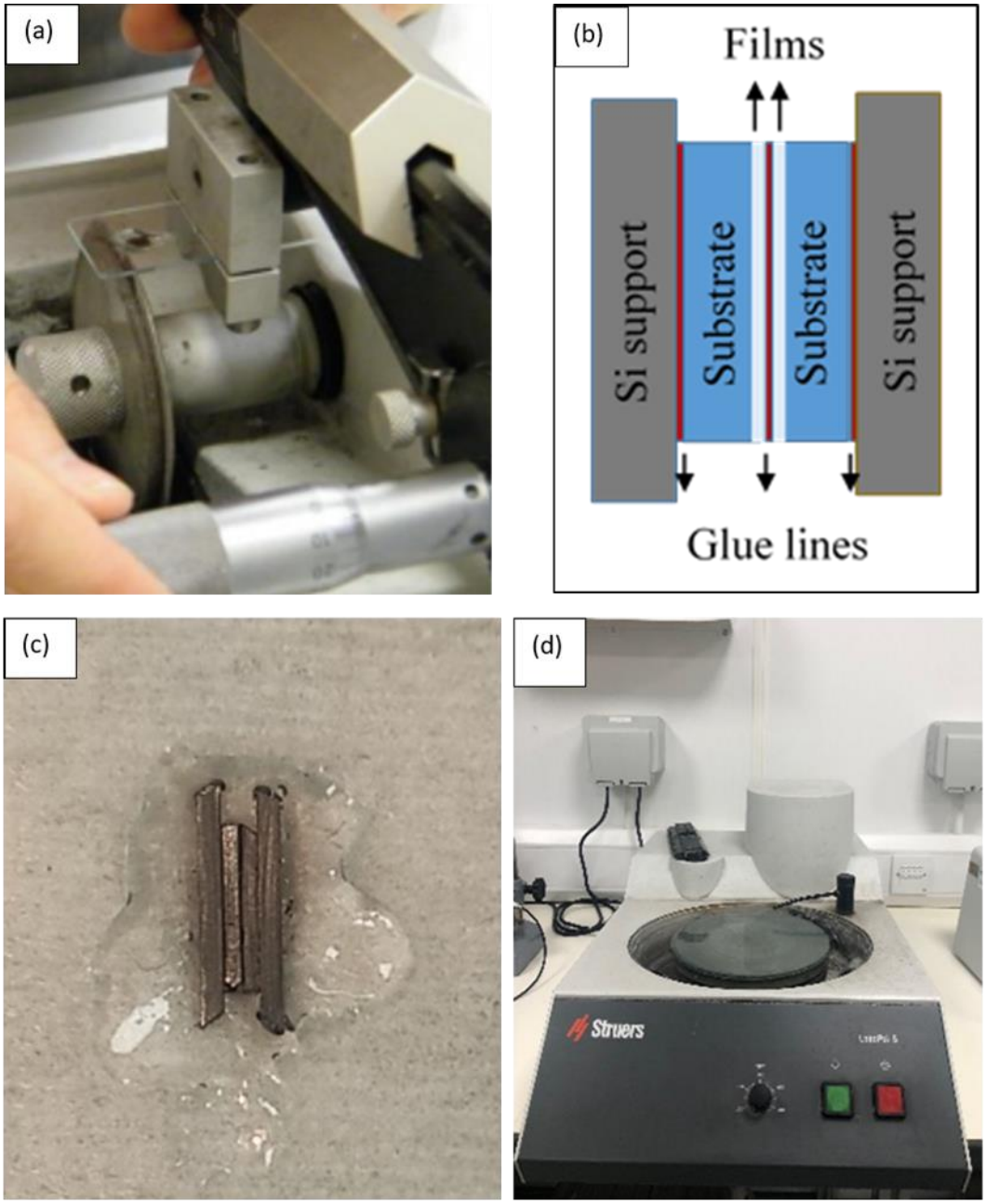

Figure 2. 19: (a) Spinning diamond-coated saw, (b) schematic representation of the specimen ready to be mechanically polished; (c) manually done specimen for polishing; (d) Polishing Instrument.

At this point, as shown in the Fig. 2.20 (a) we attach a TEM copper grid (~3 mm-diameter) to the polished surface of the specimen using the glue mixture. This ring holds the specimen once the preparation is complete and offers additional and essential mechanical support during the final polishing stage. The entire structure is then flipped over and mounted on the glass slide using Crystal Bond. The second side of the specimen is now ready to be polished.

Starting with 15 µm polishing pad the sample is thinned to 200 µm and then changes to 9 µm pad to thin the sample into 130 µm. After that by using 3µm pad the sample will be again thinned to 100 µm. After reaching this stage the final polishing step is performed with 1 µm pad to achieve a thickness below 100 µm, but the thickness is no longer checked manually but rather with an optical microscope operating in transmission mode.

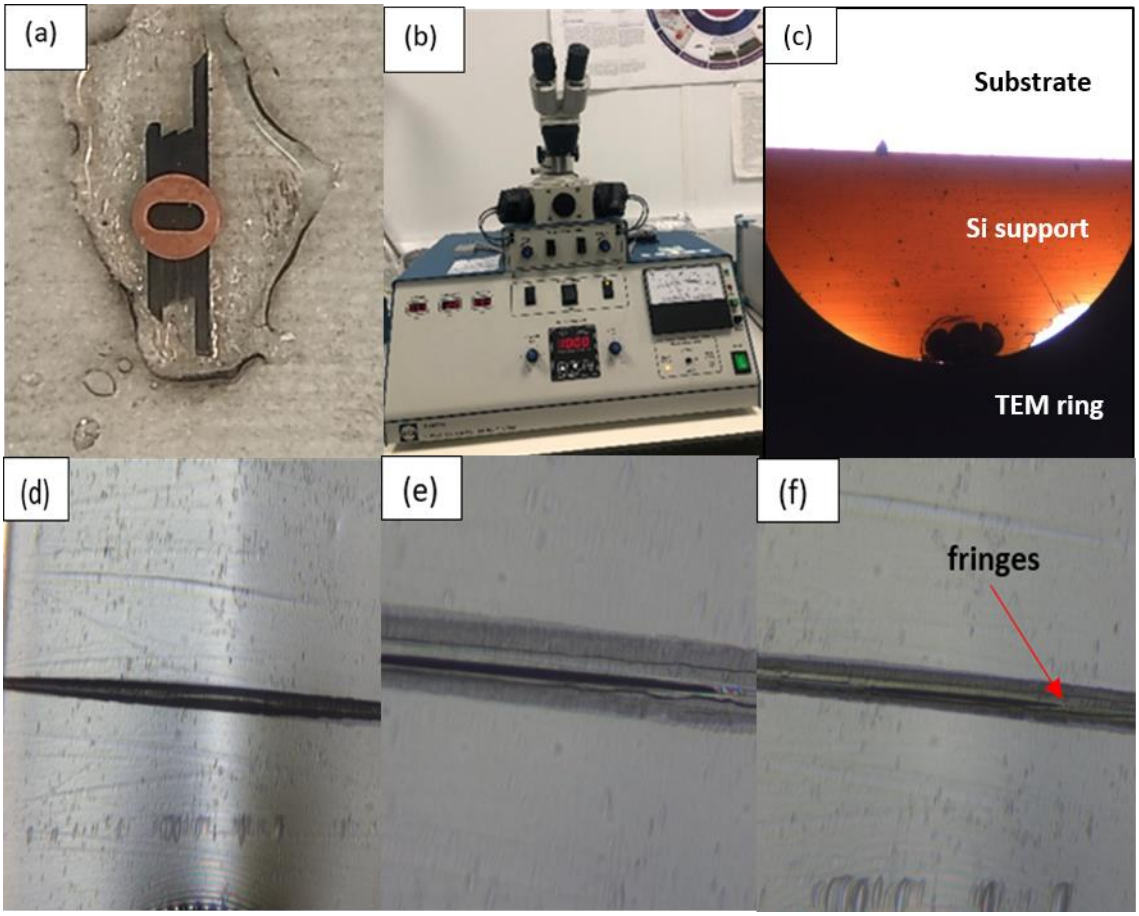

Figure 2. 20: Images showing (a) TEM copper grid glued to the polished specimen; (b) PIPS Instrument; (c) stage (Si support turns red) where the specimen is very thin and ready to be ion-milled.; (d) Hole appeared in the glue line; (e) Hole with fringes in the glue line; (f) specimen ready for microscopy studies.

As soon as the Si supports are thin enough, they start to become translucent and their colour shifts to a deep red (see Fig. 2.20 c). At this stage the manual polishing is finished and the sample is gently removed from the glass slide by heating the Crystal Bond. The sample is then put through a two-stage chemical cleaning procedure. With the help of a diamond pen, extra Si material that was protruding from the TEM grid is removed, and the sample is then ready for the next phase of the thinning procedure. The sample is about 60 µm thick which is too thin to be manually polished at this point. A Precision Ion Polishing System

(PIPS) shown in Fig. 2.20 (b) from Gatan is further used to thin the sample. Focused ion gas beams are employed by PIPS to further thin the sample until electron transparent. This device uses two guns pointed at a rotating sample stage kept in a vacuum to accelerate argon ions up to 6 keV. The guns can be rotated to produce grazing angles above and below the sample that range from 0 to 10°. The sample is milled using an accelerating voltage of 3.5 keV and an angle of ±6° until a small hole and colour fringes (Fig. 2.20 f) are visible in the glue line. The final cleaning of the sample was done inside PIPS using an accelerating voltage of 1.0 keV for 3 minutes with guns at ±8° angle, then at 0.3 keV for 10 minutes with guns at ±8° angle. The sample is now cleaned and is ready for the transmission electron microscopy studies.

2.3.2 Preparation of specimens for Scanning electron microscopy

Depending on the type of sample and the amount of information needed, sample preparation for SEM analysis can be simple or complex. Getting a sample that will fit into the SEM chamber and making a few accommodations to prevent charge build-up on electrically insulating materials count as minimal preparation. The majority of electrically insulating samples should be covered with a thin layer of conductive material on them, which is typically made of carbon, gold, or another metal or alloy. The best material for conductive coatings depends on the type of data to be collected: carbon is best for elemental analysis, whereas metal coatings work best for high-resolution electron imaging.

Chapter 3
Results and Discussions

This chapter discusses the growth and structural characterisation of as-grown and annealed Fe and Ni thin films in O_2 environment. This work aims to study and compare the single and polycrystalline structures and also to know the impact of annealing on the surface roughness of the films.

In this work, the Fe and Ni films were grown epitaxially on MgO(001) substrate (10 × 10 mm^2) using the MBE technique (as discussed in Chapter 2). Despite the difference in the lattice structure and lattice parameters (a_{Fe} = 2.866 Å and a_{MgO} = 4.212 Å) of Fe and MgO, MgO is a suitable choice of a substrate to grow Fe with a lattice mismatch of ∼4% [60]. The growth and interaction of Ni on MgO substrate are widely studied and Ni is expected to interact strongly with MgO. Some studies also report that Ni can form epitaxial relations with MgO [61-64] but the lattice mismatch of ∼16% makes it more complex and interesting at the same time.

Film growth and annealing

The MgO substrate was cleaned and prepared for growth by sonicating in an isopropanol bath for 15 minutes and annealing in the furnace at 900℃ for 1 hour. These steps remove the contaminants and make the surface flat for better deposition. The Fe and Ni films of ∼5nm thickness were deposited inside the MBE chamber by setting Fe and Ni source (in k-cells, shown in Chapter 2) temperature to 1300℃ and the substrate temperature to 250℃ respectively. The deposition was done for 50 minutes. RHEED patterns were recorded before and after the deposition of the film to observe the evolution of the surface. The samples were taken out of the chamber and a small piece (5 × 5 mm^2) from both Fe and Ni samples was annealed in-situ in the MBE chamber under a controlled temperature of 400ºC for 20 minutes with oxygen partial pressure of 5×10^{-6} mbar. RHEED was not possible after annealing due to the limitation of the size of the samples.

3.1 Structural studies of as-grown and annealed Iron (Fe) and Nickel (Ni) films on MgO (001) substrate

This section will discuss the results obtained from RHEED, SEM/EDS, and AFM of as-grown Fe and Ni films on MgO(001) and TEM, SEM/EDS, AFM results of annealed (400ºC) Fe and Ni films on MgO(001). In this work, RHEED was mainly used to monitor the sample growth and to check the surface quality of the substrate in-situ before and after the deposition of the films. The SEM (using

JEOL 7800F Prime SEM) and AFM studies were done to compare the surface morphology and roughness of both Fe and Ni films. The EDS analysis was carried out to determine the elemental composition of the materials and to study the effect of annealing on the morphology and chemical composition of the samples. TEM studies (using JEOL 2010 TEM system) on the annealed films help to determine the thickness and to have a detailed analysis of the surface morphology and crystal structure to properly understand the influence of annealing on the structure of films.

3.1.1 Fe on MgO(001) as-grown

RHEED Results

Figure. 3.1 shows the RHEED patterns acquired before and after the growth of Fe on MgO(001). The MgO substrate was cleaned and annealed before deposition to obtain a high-quality substrate with a flat surface. The sharp streaky RHEED pattern taken from MgO(001) substrate as shown in Fig. 3.1 (a) confirms that a flat surface with small domains was obtained. As observed in Fig.3.1 (b), the RHEED results after deposition of the Fe film on MgO(001) show a modulated streaky pattern, which indicates that the Fe film has surface roughening (e.g. a multilevel stepped surface). The streaks in RHEED represent the epitaxial growth of a single crystal, while the modulated intensity can be interpreted by the electron transmission through small grains [65, 66].

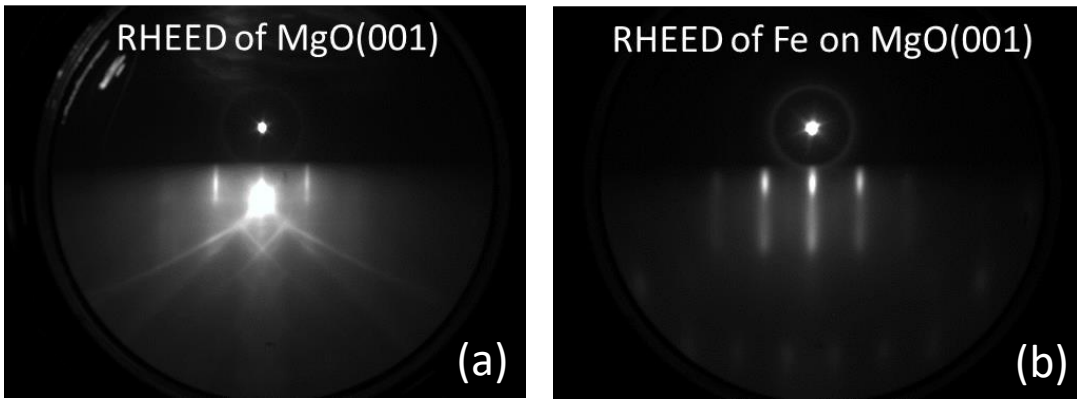

Figure 3. 1: RHEED patterns acquired (a) from MgO(001) surface before deposition of the Fe film, results in a sharp streaky pattern that confirms the high quality of the substrate with a flat surface (b) after deposition of Fe film on MgO(001) showing a modulated streaky pattern, which indicates that the Fe film has surface roughening, i.e., a multilevel stepped surface.

SEM Results

The surface morphology of as-grown Fe film on MgO(001) taken using a LED detector at both low and high acceleration voltage (5 kv & 15 kv) is shown in Fig. 3.2. The low-resolution image of the sample with an acceleration voltage of

5 kv presented in Fig 3.2 (a) shows that the sample exhibits a rough surface which is less organised and non-uniform. Some contamination (dust) on top of the sample becomes visible with the lower voltage. The images of the sample shown in Fig. 3.2 (b) at a higher voltage of 15 kv and in Fig. 3.2 (c) with a voltage of 5 kv, also show the surface roughening and presence of dust-like particles on the film surface. The higher resolution images of the as-grown Fe film surface shown in Fig. 3.2 (d-f) confirm that the surface morphology of the Fe film is composed of small domains and stepped surfaces which support the RHEED results [67]. This rough surface may be attributed to the contamination or dust particles from the carbon tape used to hold the sample in the SEM/EDS stub or it can be also due to the influence of lattice mismatch between Fe and MgO [60]. Further investigation on the surface roughness and elemental composition was done using AFM and EDS which is described later.

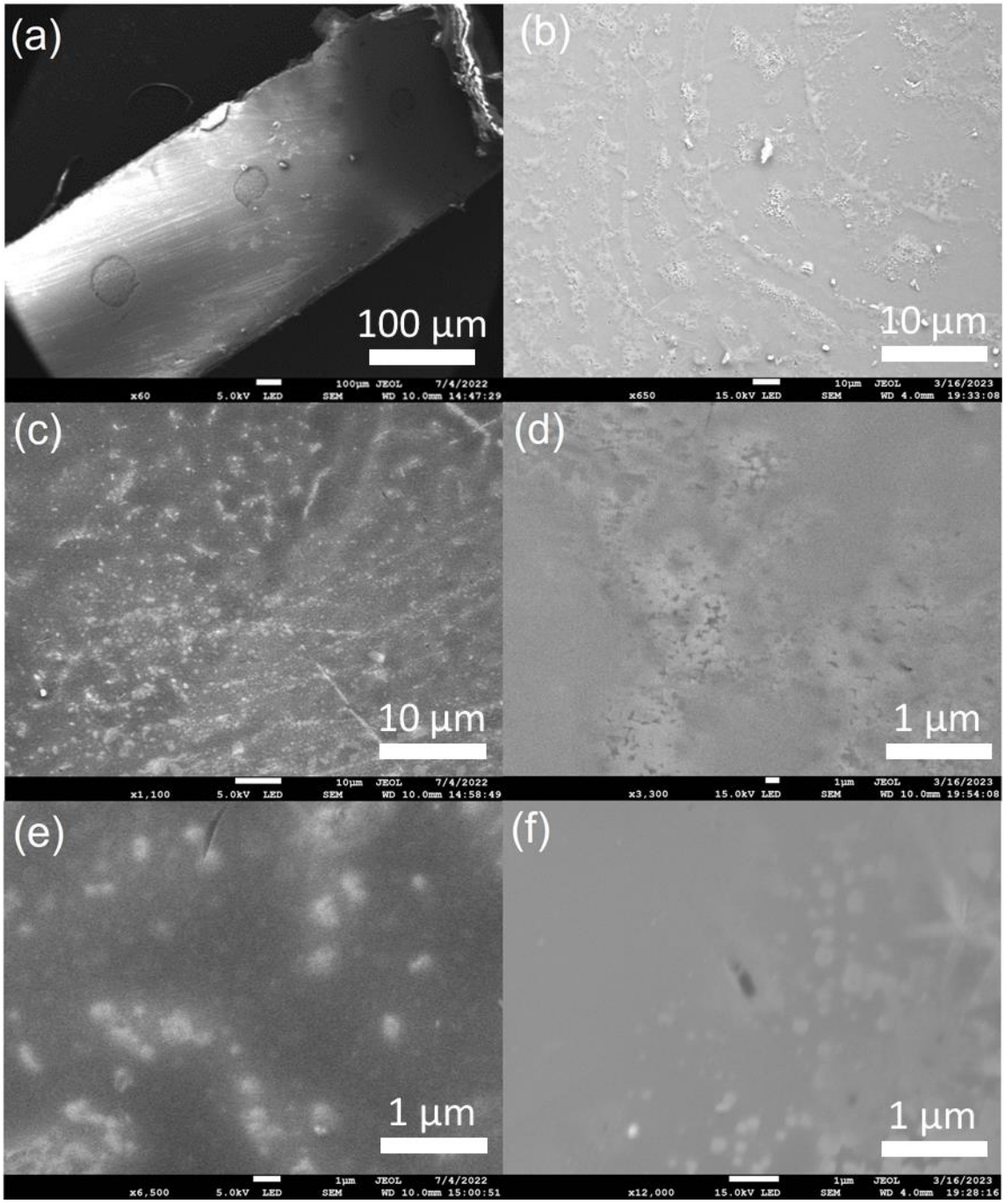

Figure 3. 2: SEM images (top view) showing the surface morphology of as-grown Fe film on MgO (001) taken using LED detector at different working distance of 4 & 10mm (a) image of as-grown Fe film at lower magnification with an acceleration voltage of 5 kv (scale bar:100 µm) showing a rough surface, (b & c) surface of as-grown Fe film at increased magnification with a scale bar of 10 µm showing the surface roughening and presence of dust like particles, (d, e & f) images showing the surface of as-grown Fe film at increased magnification and acceleration voltage (5 kv & 15 kv) with a scale bar of 1 µm confirm that the surface morphology of the Fe film is composed of small domains and stepped surfaces.

AFM Results

The topography and surface morphology of the as-grown Fe films on MgO(001) substrate were given by the AFM analysis (shown in Fig. 3.3) which is in good agreement with the SEM results. Fig 3.3 (a) gives the two-dimensional (2D) or plane-view of surface roughness for the as-grown Fe films. The 3D view of the surface roughness of the film is shown in Fig. 3.3 (b). The film shows a rough, stepped surface (Fig. 3.3 b) and the root-mean-square (RMS) surface roughness value of the film is found to be 0.91 nm.

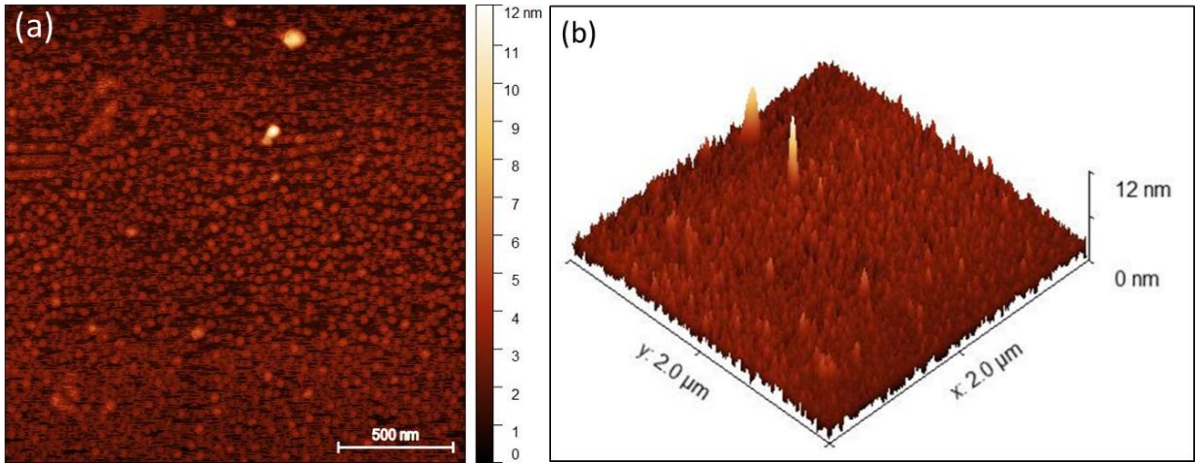

Figure 3. 3: AFM images showing the topography of as-grown Fe on MgO(001) film with a scan area of 2 × 2 μm^2 (a) 2-dimensional view, (b) 3-dimensional view.

EDS Results

The EDS analysis was done to confirm the elements in the sample. The results from EDS analysis of as-grown Fe on MgO(001) film (particles with dimensions around 10µm) are shown in Fig. 3.4. The selected area for mapping and spectrum analysis is shown in Fig. 3.4 (a). The results of elemental mapping (shown in Fig. 3.4 b & c) confirms the presence of the elements Mg and O from the substrate and Fe from the film. The presence of C (as shown in Fig. 3.4 c) is related to the impurities (suspected to have come from dust or from the carbon tape used to hold the sample in the SEM/EDS stub) on the film. EDS spectra from the film, normalised to Mg K-Peak, are shown in Fig. 3.4 (d), revealing the peaks of Mg, O, and Fe along with the impurities C. The atomic composition of the elements according to the spectrum analysis is Mg = 35%, O_2 = 43.2 %, Fe = 0.5%, and C = 21.3%. These results confirm that there was a presence of >20% impurity on the film surface which might have led to the rough surface as seen in SEM results.

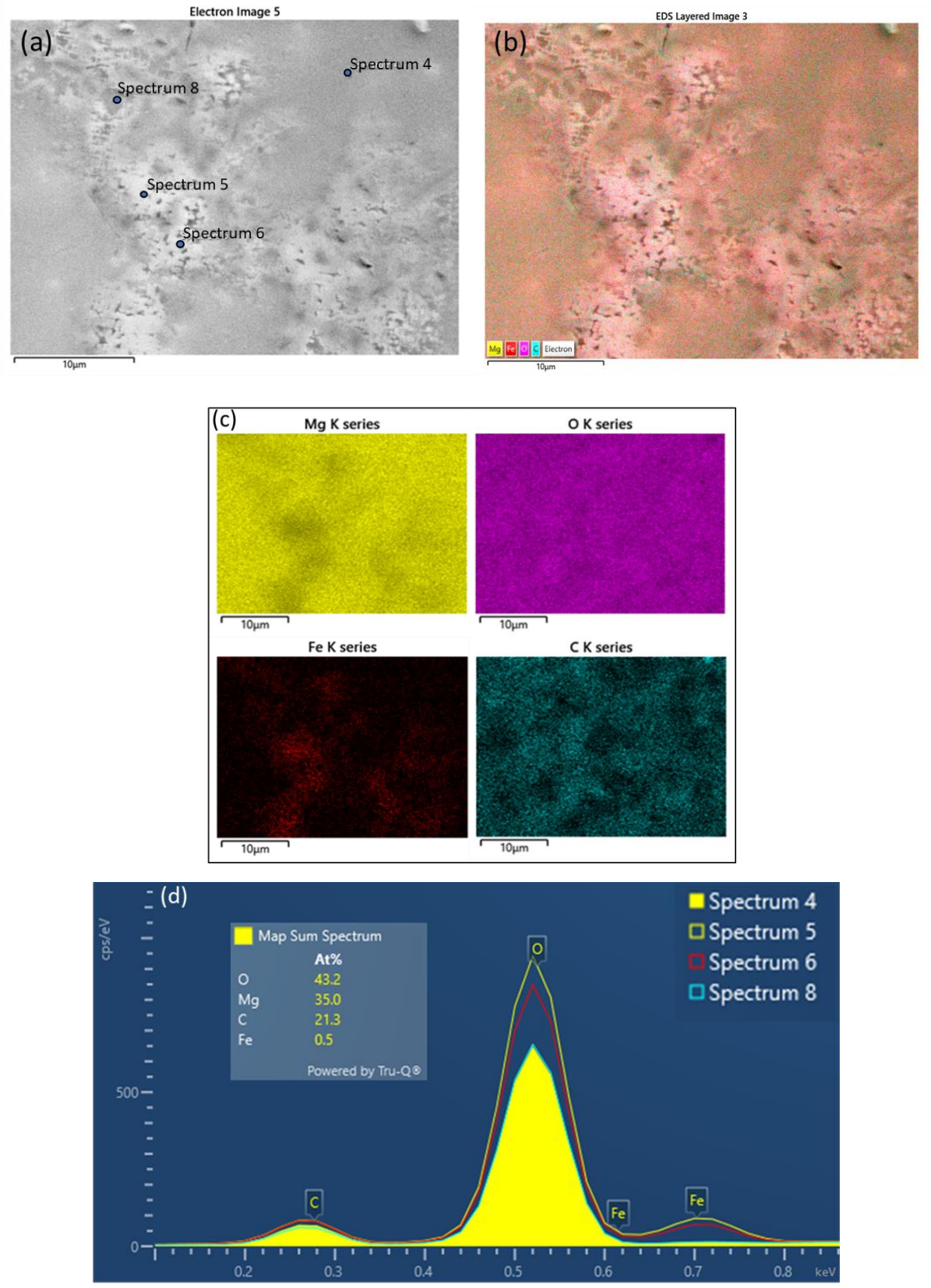

Figure 3. 4: EDS results of as-grown Fe on MgO(001) showing (a) selected area for mapping and spectrum analysis, (b & c) elemental mapping results confirming the presence of the elements Mg and O from the substrate, Fe from the film and also the presence of C on the surface, (d) spectrum analysis showing the sum spectrum and atomic percentage of each element in the film.

3.1.2 Fe on MgO(001) annealed at 400°C

SEM Results

SEM surface analysis of the Fe film on MgO(001) after annealing (in-situ) at 400°C is shown in Fig. 3.5. The image of the sample at low-magnification with an acceleration voltage of 20 kv is shown in Fig 3.5 (a & b). A noticeable change in the surface morphology has been observed after annealing. The surface of the Fe film seems more uniform after annealing than the as-grown Fe films on MgO(001). As seen in Fig. 3.5 (c & d) the film surface shows darker spots due to hydrocarbon contamination. This contamination on the sample surface becomes more visible in the higher-resolution images with a lower acceleration voltage of 5 kv (as shown in Fig. 3.5 e & f). Further investigation on the sample was done using AFM and TEM analysis which is described later.

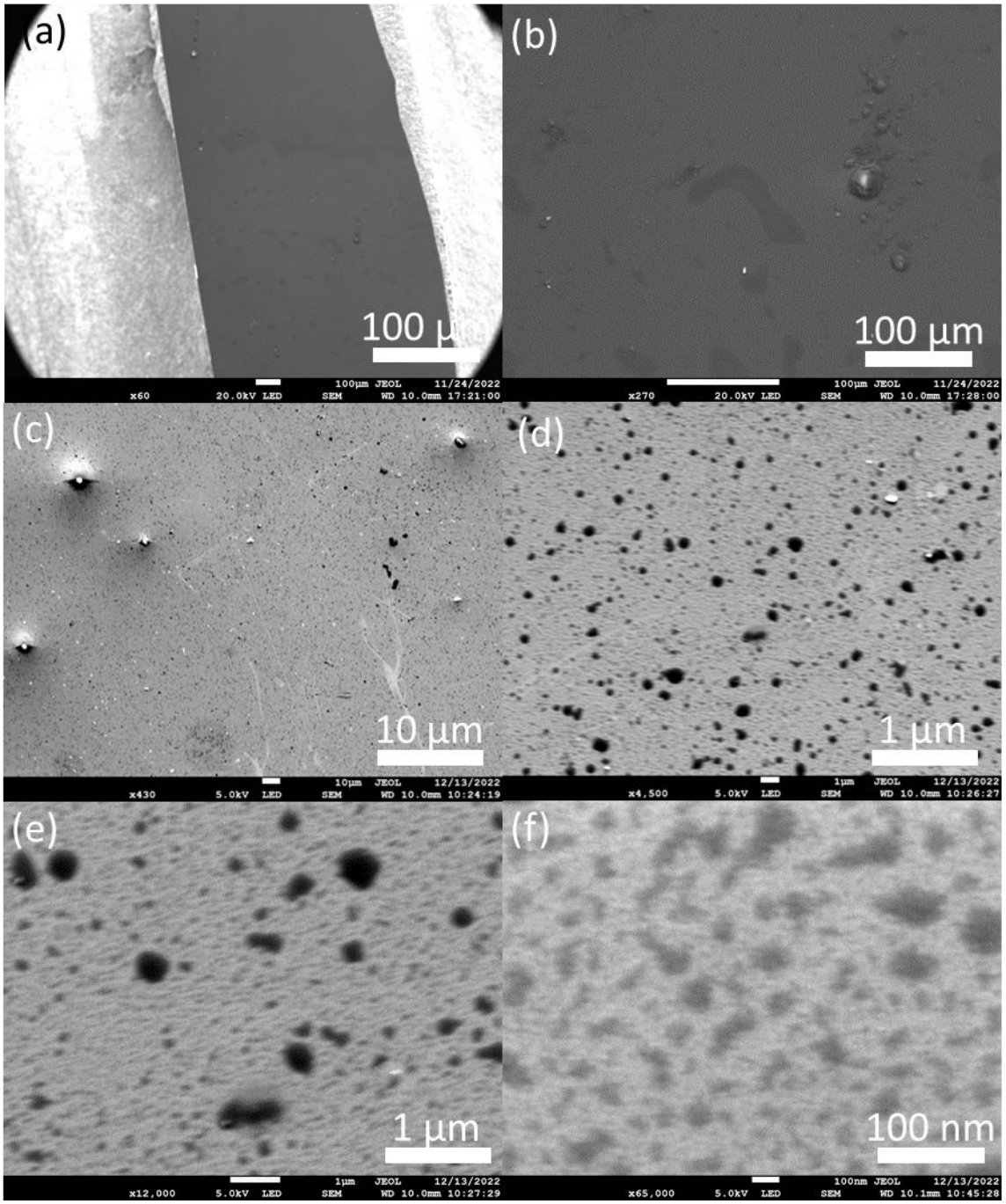

Figure 3. 5: SEM images (top view) showing the surface morphology of Fe on MgO(001) annealed at 400°C taken using LED detector at a working distance of 10mm (a & b) images of annealed Fe film at lower magnification with an acceleration voltage of 20 kv (scale bar :100 µm) showing a uniform surface compared to the as-grown Fe film surface, (c & d) uniform surface of annealed Fe film at increased magnification showing darker spots due to hydrocarbon contamination, (e & f) high resolution images with a lower acceleration voltage of 5 kv where the contamination due to the carbon is more visible.

AFM Results

The AFM results revealing the topography of annealed (400°C) Fe on MgO(001) film are shown in Fig. 3.6 (a & b). There seems a tremendous change in the surface morphology of the annealed films as compared to the as-grown samples (shown in Fig. 3.3). Fig 3.6 (a) gives the two-dimensional (2D) or plane-view of surface roughness for the annealed Fe films. The 3D view of the surface roughness of the film is shown in Fig. 3.6 (b). A dramatic rise in the surface roughness is seen in the topography image (shown in Fig. 3.6 b). The RMS surface roughness increased with annealing. The annealed films show a root-mean-square (RMS) roughness of 3.30 nm which is more than thrice the surface roughness of as-grown (0.91 nm) Fe samples. The increase in surface roughness can be due to grain growth and film crystallisation. But in this case, such a huge rise in the roughness is thought to be the result of carbon contamination as seen in SEM analysis.

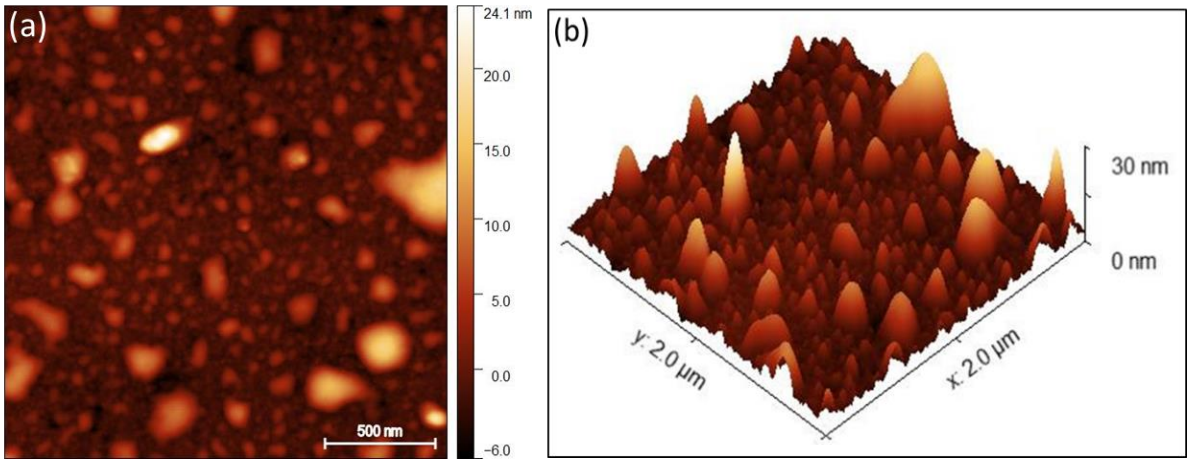

Figure 3. 6: AFM images showing the topography of annealed Fe on MgO(001) film at 400°C with a scan area of 2 × 2 μm^2 (a) 2-dimensional view, (b) 3-dimensional view.

EDS Results

The chemical composition of the film was revealed by EDS mapping and spectrum analysis which is shown in Fig. 3.7. The selected area for mapping and spectrum analysis is shown in Fig. 3.7 (a). The elemental mapping (as shown in Fig. 3.7 b & c) showed that the annealed film mainly consists of uniformly distributed Mg, O, and Fe along with C. As mentioned earlier the presence of carbon signals is from hydrocarbon contamination on the surface.

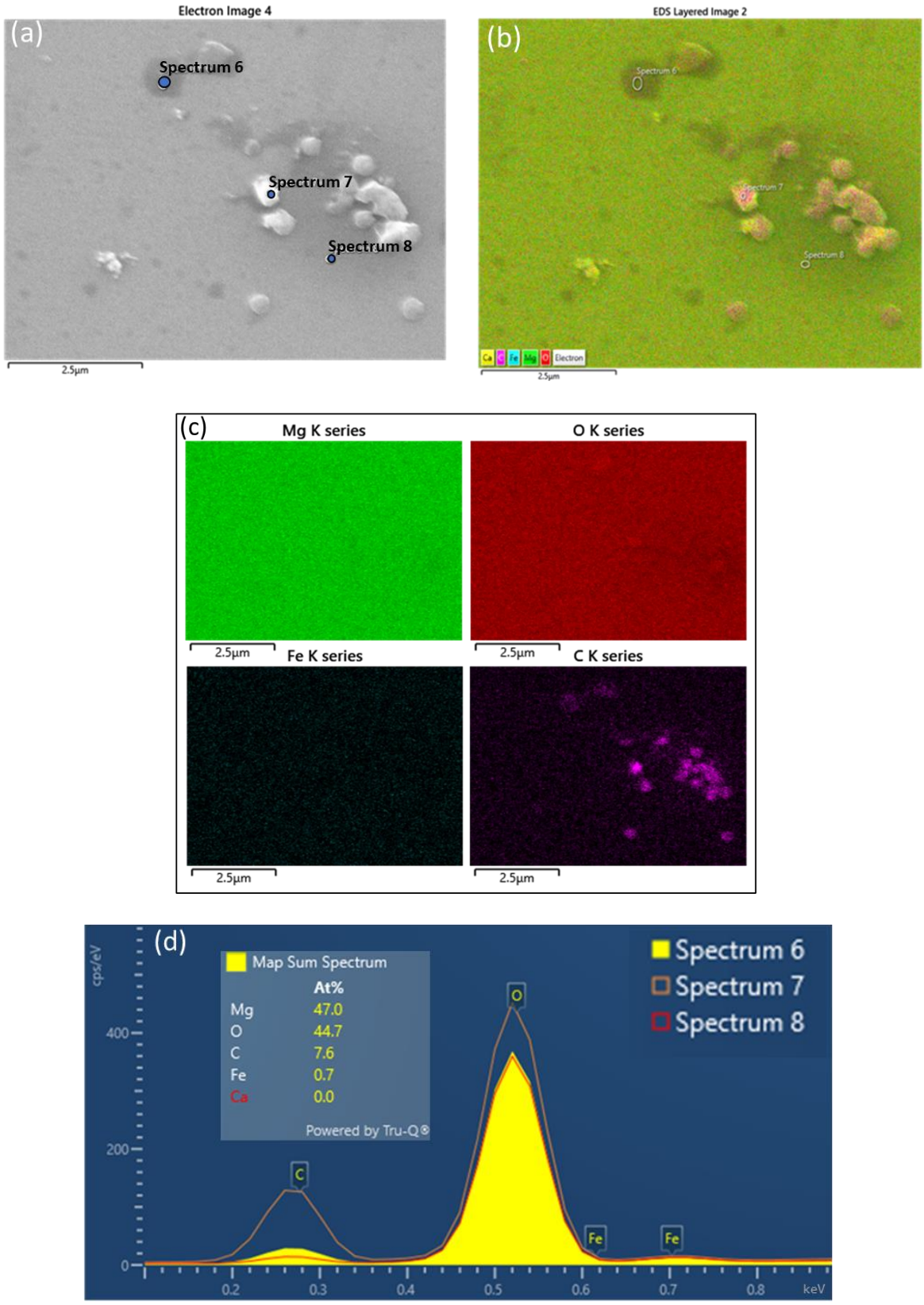

Figure 3. 7: EDS results of Fe on MgO(001) annealed at 400℃ showing (a) selected area for mapping and spectrum analysis, (b & c) elemental mapping results confirming the presence of the elements Mg and O from the substrate, Fe from the film and also the presence of C on the surface, (d) spectrum analysis showing the sum spectrum and atomic percentage of each element in the film.

The EDS spectra (shown in Fig. 3.7 d) reveal the peaks of the elements in the film. Comparing the spectrum, it is realised that particles on the surface selected for spectrum 7 show more presence of carbon than the area chosen for spectrum 6 & 8. This confirms the presence of contamination on the film surface which might be the cause of film roughness (which supports the AFM results). We can see an increase in the oxygen peak in spectra 7. Comparing the atomic percentage of the elements (shown in Fig 3.7 d), there is a small rise in the amount of oxygen in the annealed films to the as-grown Fe films (shown in Fig. 3.4 d). The overall increase in oxygen percentage to 44.7% might be the effect of further film oxidation due to in-situ annealing. This was further investigated in the TEM analysis.

TEM Results

Fig 3.8 displays the low and high magnification TEM images of the cross-sectional Fe films annealed (20 min) at 400℃. The TEM images show two separate layers of thickness ~4.18 nm and ~5 nm respectively. In the following, we will demonstrate that these two layers are non-oxidised (lower layer) and oxidised iron (upper layer). Fig. 3.8 (c & d) shows a clear planar interface between the substrate and the film.

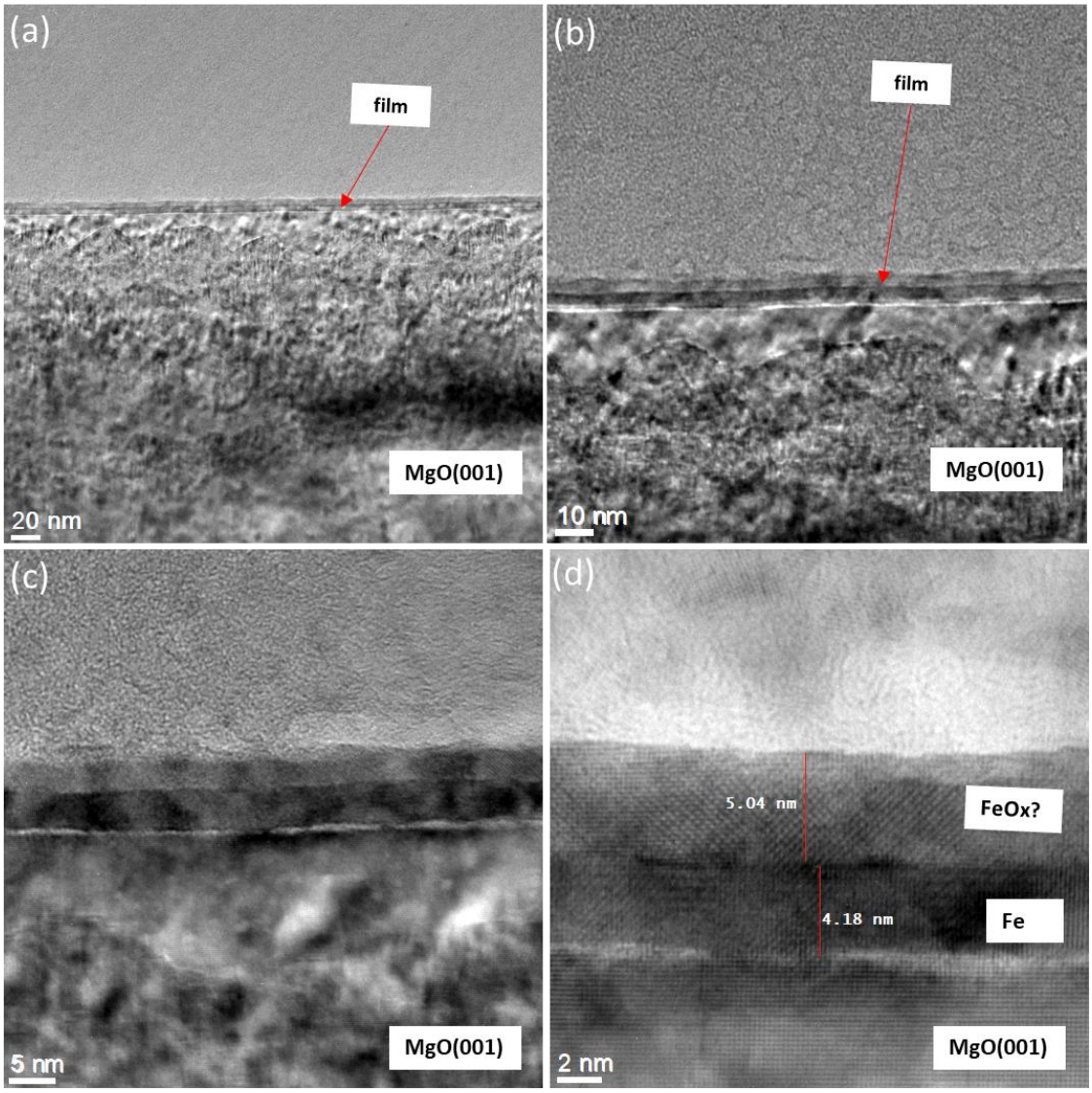

Figure 3. 8: Cross-sectional Bright-Field (BF) low and high magnification TEM images of Fe on MgO(001) annealed for 20 min at 400°C, showing (a, b & c) clear interface between the substrate and the film Fe with a small layer of oxidised Fe on top, (d) HRTEM image showing non-oxidised Fe with a layer of oxidised iron FeO_x of thickness ~4.18 nm and ~5 nm respectively.

The lattice d-spacing analysis performed using FFT diffractograms (using JEMS software from the HRTEM images (shown in Fig 3.9) could prove that the top layer is Fe_3O_4 along [001] zone axis and the non-oxidised layer of Fe is along [101] zone axis. Fig. 3.10 shows the analysis (using JEMS software) of the selected area electron diffraction (SAED) pattern obtained from the annealed Fe films showing the single crystalline Fe [101] and Magnetite (Fe_3O_4) [001] on MgO(001).

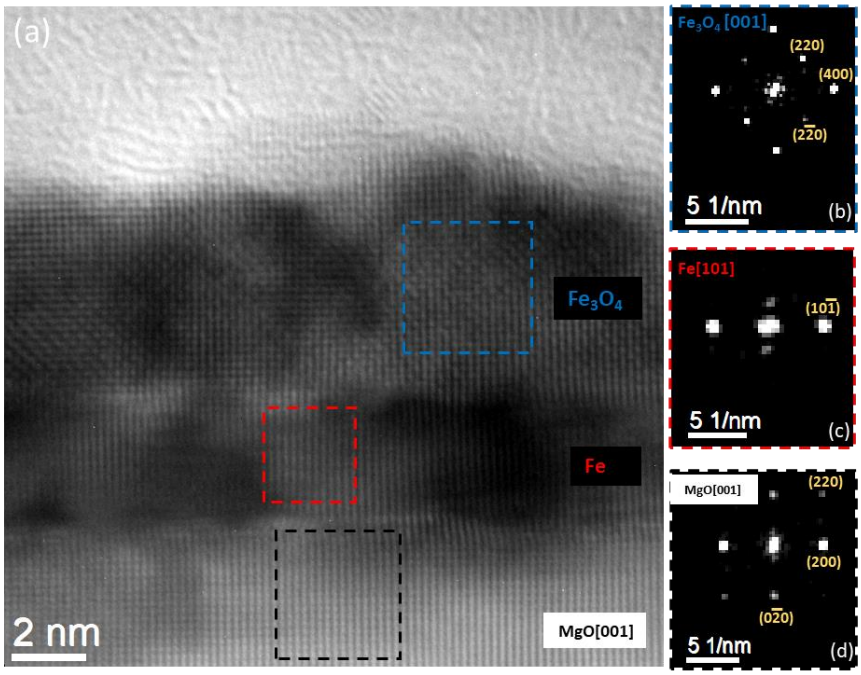

Figure 3. 9: **(a)** HRTEM image of Fe on MgO (001) annealed at 400°C comprising of area chosen for the lattice d-spacing analysis of substrate MgO (black dashed box), Non-oxidised Fe (red dashed box), Fe_3O_4 (blue dashed box); **(b)** FFT diffractogram of Fe_3O_4[001]; **(c)** FFT diffractogram of Fe [101]; **(d)** FFT diffractogram of MgO [001].

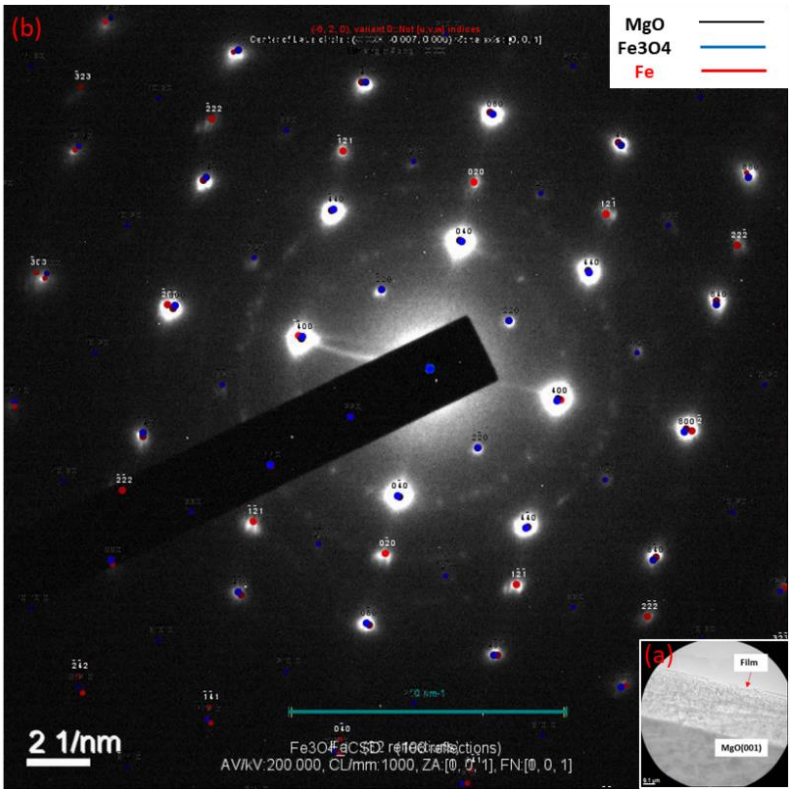

Figure 3. 10: (a) Selected area for the diffraction pattern from the substrate MgO(001) and film; (b) Analysed SAED pattern showing the single crystalline growth of Fe [101] (red spots), and Magnetite (Fe_3O_4) [001] (blue spots); on MgO(001) (black spots).

3.1.3 Ni on MgO (001) as-grown

RHEED Results

Fig. 3.11 (a) Shows the RHEED pattern acquired from the MgO(001) substrate before the deposition of the film. The sharp streak pattern in RHEED indicates that the substrate has a high-quality, flat surface with small structural domains. The RHEED pattern obtained after deposition of the Ni film on MgO(001) is shown in Fig. 3.11 (b). The streaky pattern obtained after the deposition of the film indicates an epitaxial growth. Additional diffraction rings (shown in Fig. 3.11 c) appeared which are less visible (marked for reference) representing the polycrystalline growth of the film [66].

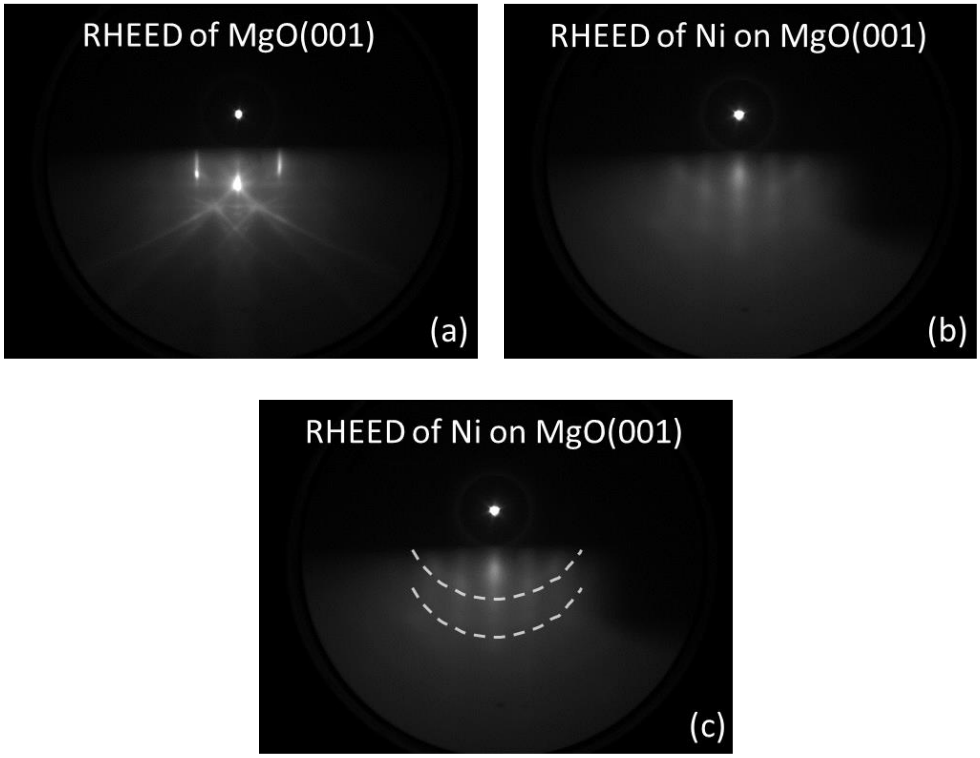

Figure 3. 11: Experimental RHEED patterns from (a) MgO(001) surface before deposition of the film, (b) after deposition of Ni film on MgO (001), (c) image of after deposition of Ni film showing the diffraction rings (marked by dashed lines for reference).

SEM Results

Fig. 3.12 shows the surface morphology of as-grown Ni film on MgO(001). The sample exhibits a highly rough surface compared to as-grown Fe films (shown in Fig. 3.2). The image of the sample at low magnification with an acceleration voltage of 20 kv is shown in Fig 3.12 (a & b). The image of the film surface shown in Fig. 3.12 (c to f) consists of a granular structure [68]. It seems like the sample has a polycrystalline structure (Fig. 3.12 e & f) as suggested by the

RHEED results. The surface is non-uniform and the particles (grains) are clustered together unlike the as-grown Fe film surface. The high rough surface seems to be the result of the clustering of the grains and film crystallisation. The carbon contamination as seen earlier can also induce surface roughness. This was further investigated in the EDS analysis.

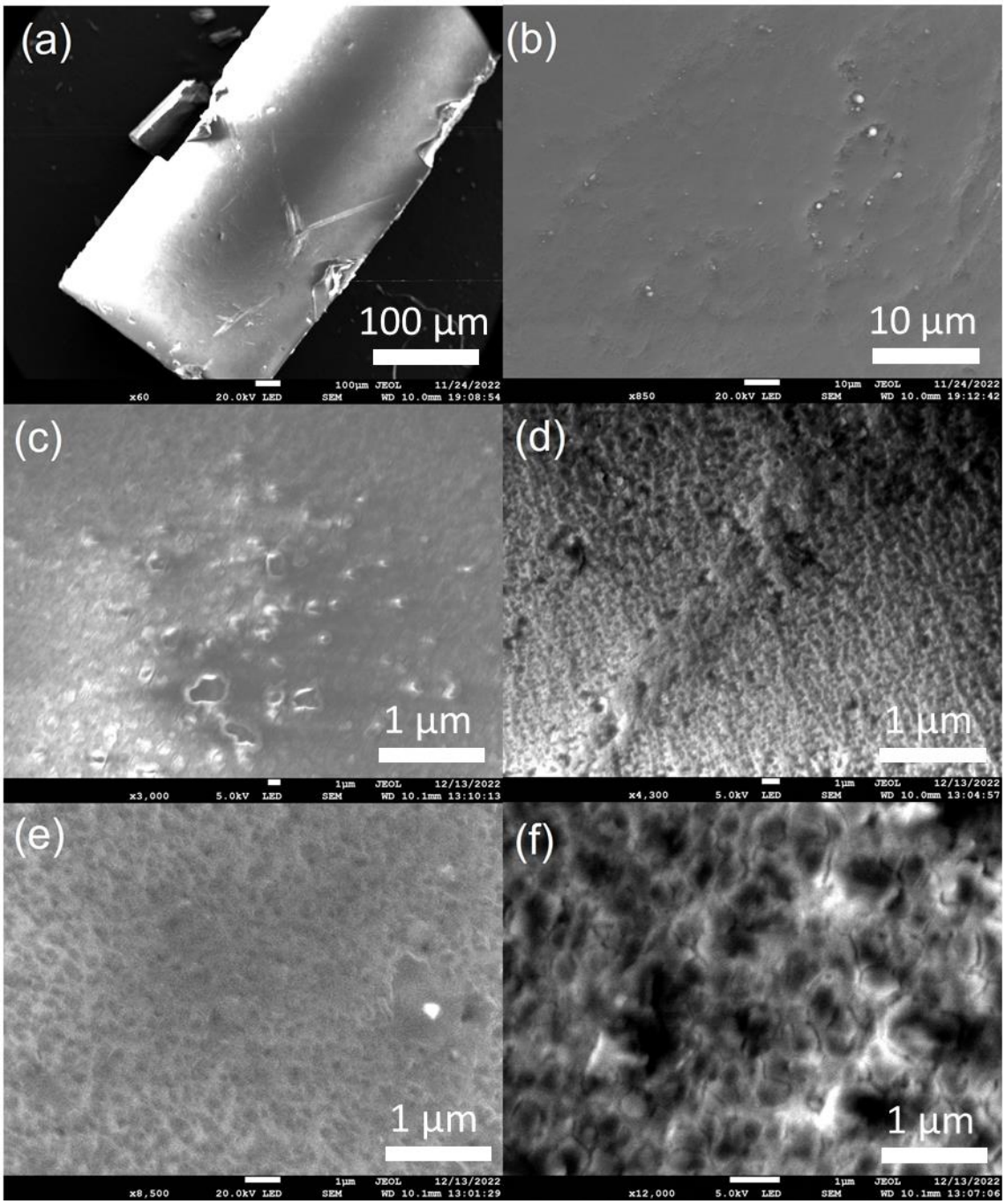

Figure 3. 12: SEM images (top view) showing the surface morphology of as-grown Ni on MgO(001) films taken using an LED detector at a working distance of 10mm (a & b) images at lower magnification with an acceleration voltage of 20 kv, (c & d) images with a lower acceleration voltage of 5 kv showing a granular structure on the film surface, (e & f) high-resolution images exhibiting a highly rough surface and seems like the particles (grains) are clustered together.

AFM Results

The AFM topography images of as-grown Ni films are shown in Fig. 3.13 which is in good agreement with the SEM results. The AFM results indicate that the film shows a non-uniform and stepped surface with root-mean-square (RMS) roughness of 1.61 nm. Fig 3.13 (a) gives the two-dimensional (2D) view of surface roughness for the as-grown Ni films. The 3D view of the surface roughness of the film is shown in Fig. 3.13 (b). This result confirms that the Ni film surface is rougher than the Fe film surface, which is, considered to be the result of the clustering of the grains.

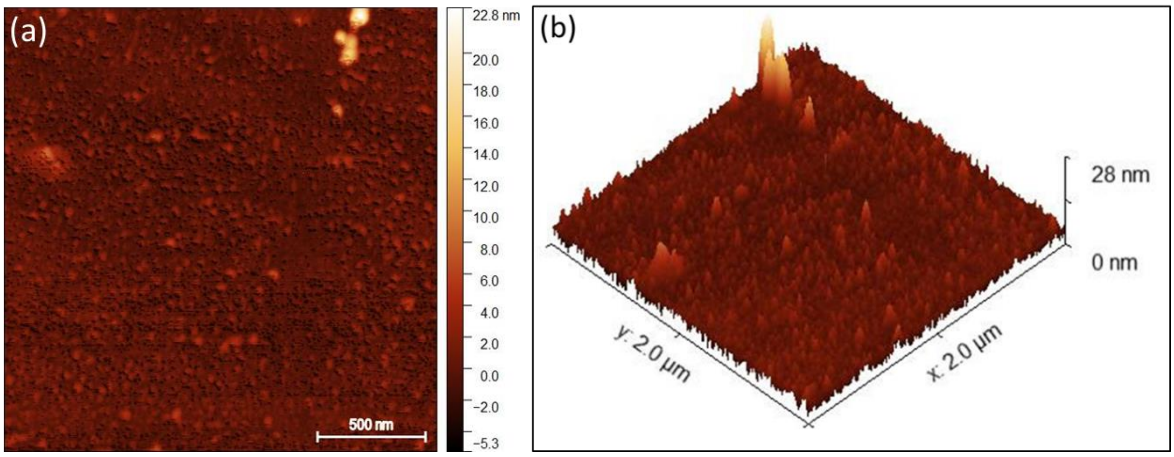

Figure 3. 13: AFM images showing the topography of as-grown Ni on MgO(001) film with a scan area of $2 \times 2\ \mu m^2$ (a) 2-dimensional view, (b) 3-dimensional view.

EDS Results

Fig. 3.14 shows the EDS elemental mapping and spectrum analysis of the as-grown Ni on the MgO(001) sample. The selected area for mapping and spectrum analysis is shown in Fig. 3.14 (a). The elemental mapping (Fig. 3.14 b & c) confirms the presence of the elements (non-uniform distribution) Mg and O from the substrate and Ni from the film. A small carbon signal was also present which can be related to the impurities on the film similar to the Fe films. The EDS spectra (shown in Fig. 3.14 d) reveal the peaks of Mg, O, and Ni along with C. The atomic composition of Ni is shown as 0.5%. The oxygen peak is almost similar in spectra 1 & 3. The rise of the oxygen peak in spectrum 2 is from the contaminants.

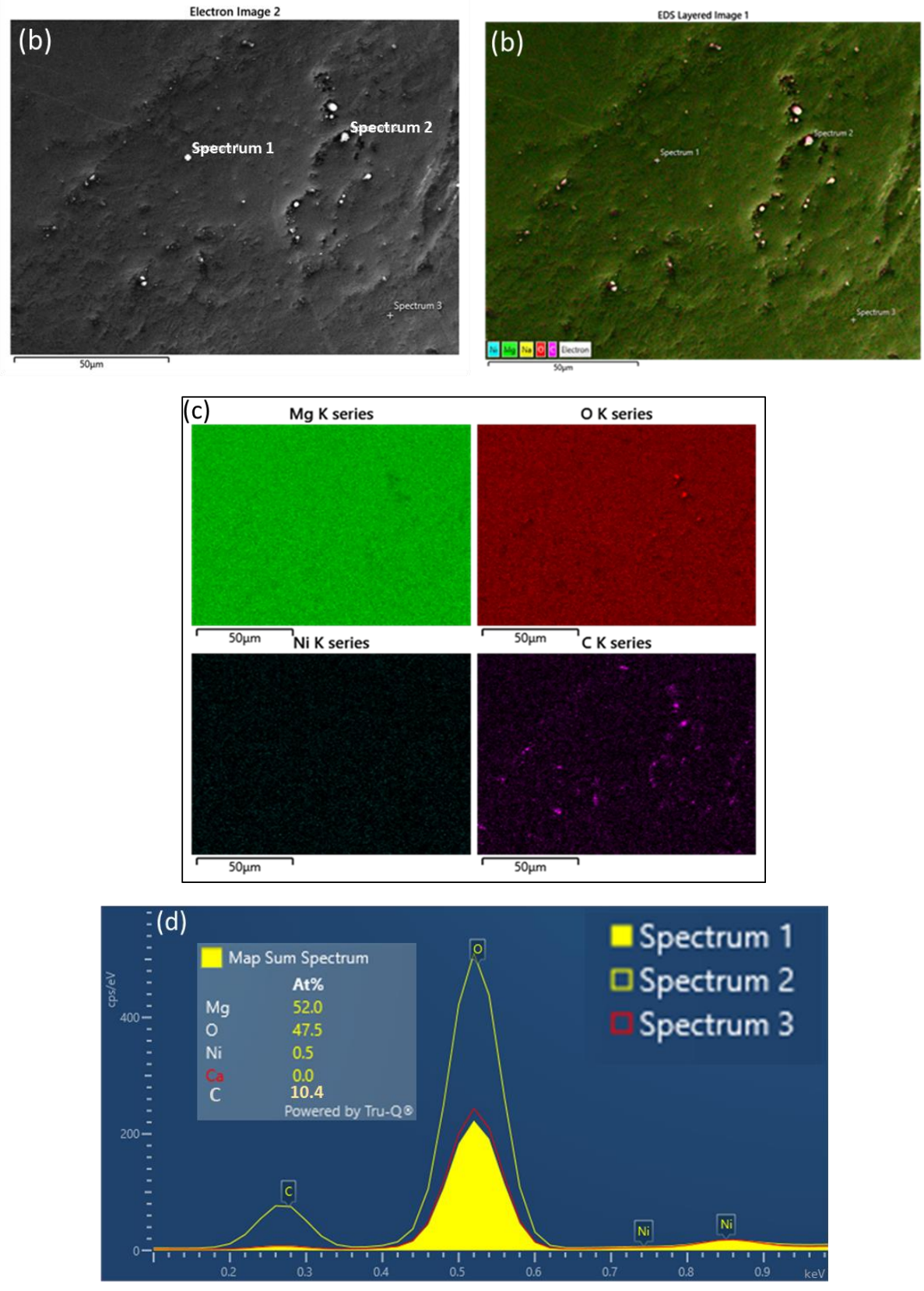

Figure 3. 14: EDS results of as-grown Ni on MgO(001) showing (a) selected area for mapping and spectrum analysis, (b & c) elemental mapping results confirming the presence of the elements Mg and O from the substrate, Ni from the film and also the presence of C on the surface, (d) spectrum analysis showing the sum spectrum and atomic percentage of each element in the film.

3.1.4 Ni on MgO (001) annealed at 400°C

SEM Results

SEM images showing the surface analysis of the annealed (in-situ) Ni on MgO(001) film at 400°C are shown in Fig. 3.15. The surface of the sample at low magnification with a high acceleration voltage of 20 kv is shown in Fig 3.15 (a & b). The bubble-like structure seen in Fig 3.15 (b) must be carbon clustering. The image of the annealed Ni film surface appears rougher in Fig. 3.15 (c to f) than the as-grown Ni films. Similarly, to Fe samples, a significant change in surface morphology has been seen in Ni films after annealing. But the Ni surface is rougher than the surface of Fe film (Fig. 3.5), after the annealing. It can be said that the annealing increases roughness.

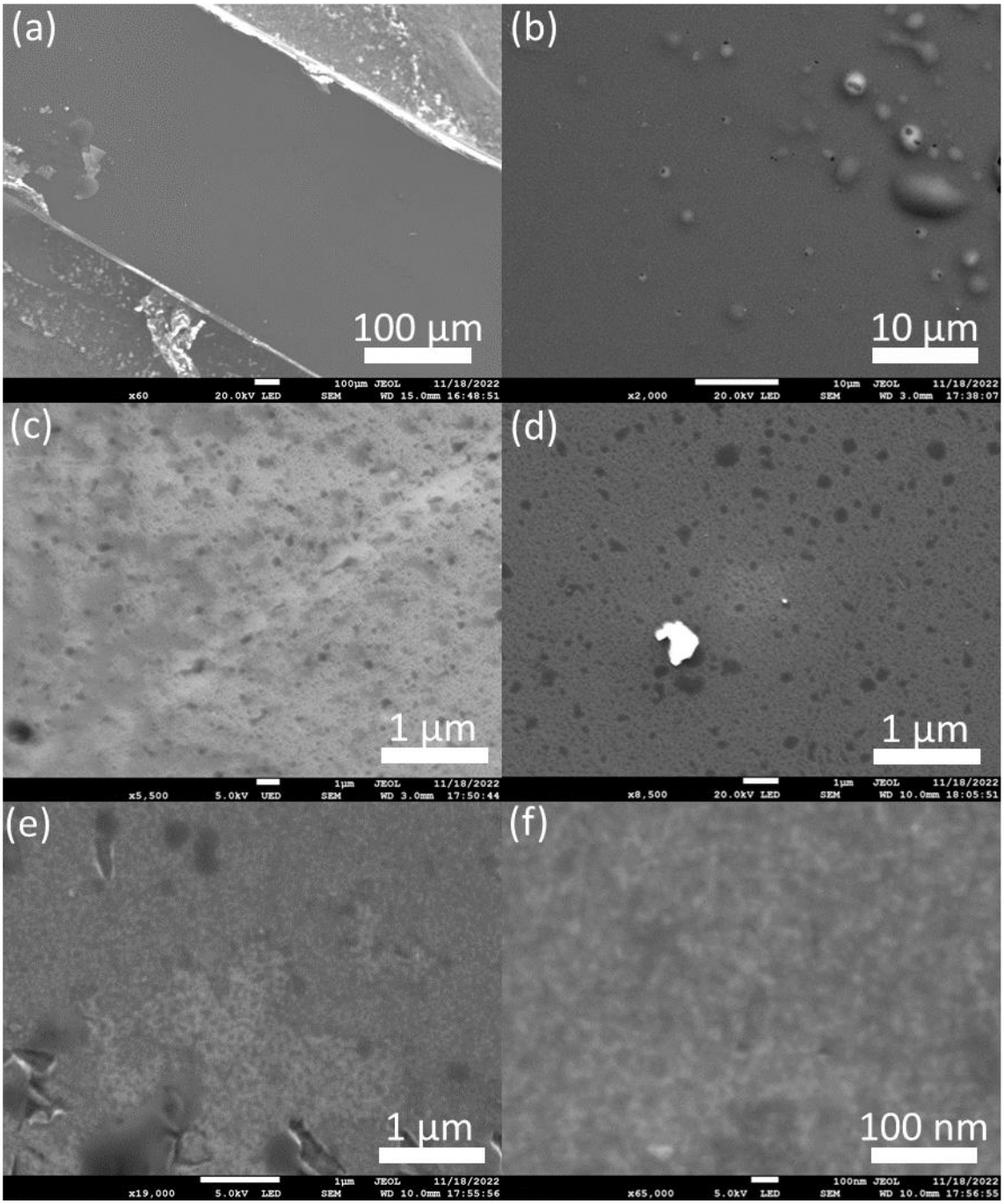

Figure 3. 15: SEM images (top view) showing the surface morphology of Ni on MgO(001) annealed at 400℃ (a & b) images at lower magnification with an acceleration voltage of 20 kv, (c to f) lower and high-resolution images exhibiting a highly rough surface of annealed Ni films.

AFM Results

The AFM results shown in Fig. 3.16 (a & b) reveal the surface topography of annealed Ni films. A drastic change in the morphology was seen in the AFM results. As compared to the as-grown Ni samples (RMS roughness=1.61 nm)

there seems a huge rise in the surface roughness after annealing. The root-mean-square (RMS) roughness of 4.61 nm from the AFM analysis indicates that the surface roughness of the Ni samples increased significantly with annealing. The grain growth induced by annealing makes the film rougher and may have induced the crystallinity. The AFM analysis could also confirm that Ni films are rougher compared to Fe films.

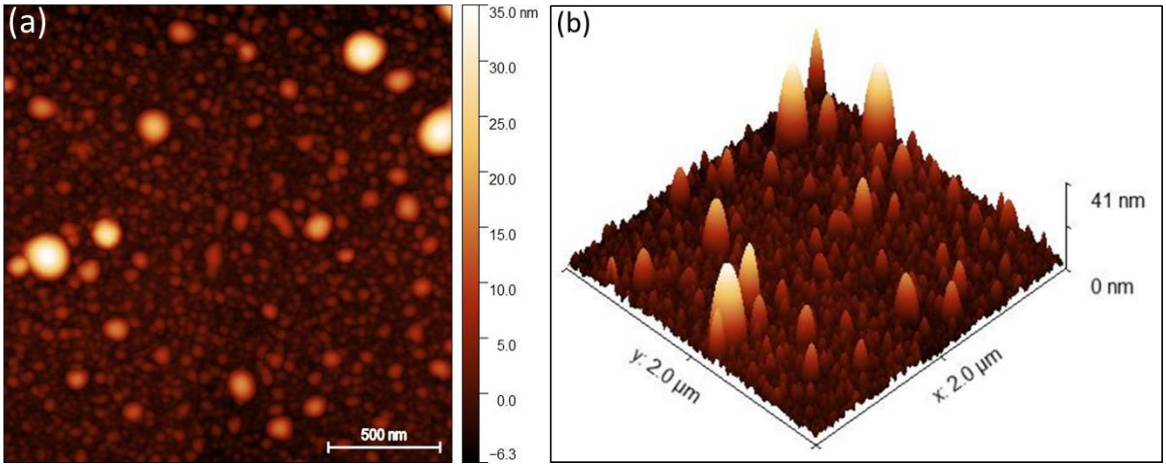

Figure 3. 16: AFM images showing the topography of annealed Ni on MgO(001) film at 400°C with a scan area of 2 × 2 μm^2 (a) 2-dimensional view, (b) 3-dimensional view.

EDS Results

Fig. 3.17 reveals the chemical composition and spectrum analysis of the annealed Ni film. Fig. 3.17 (a) shows the selected area for mapping and spectrum analysis. The EDS mapping and spectrum analysis (shown in Fig. 3.17 b & c) consist of Mg, O, and Ni from the film along with C from contamination on the surface. The oxygen peak varies in every spectrum as shown in Fig. 3.17 (d). The rise of the oxygen peak in each spectrum is from the contaminants. There was no visible change in the atomic percentage of oxygen in the annealed Ni films to the as-grown films which can explain the effect of annealing (oxidation) like Fe films (shown in Fig. 3.7 d). This was further investigated in the TEM analysis.

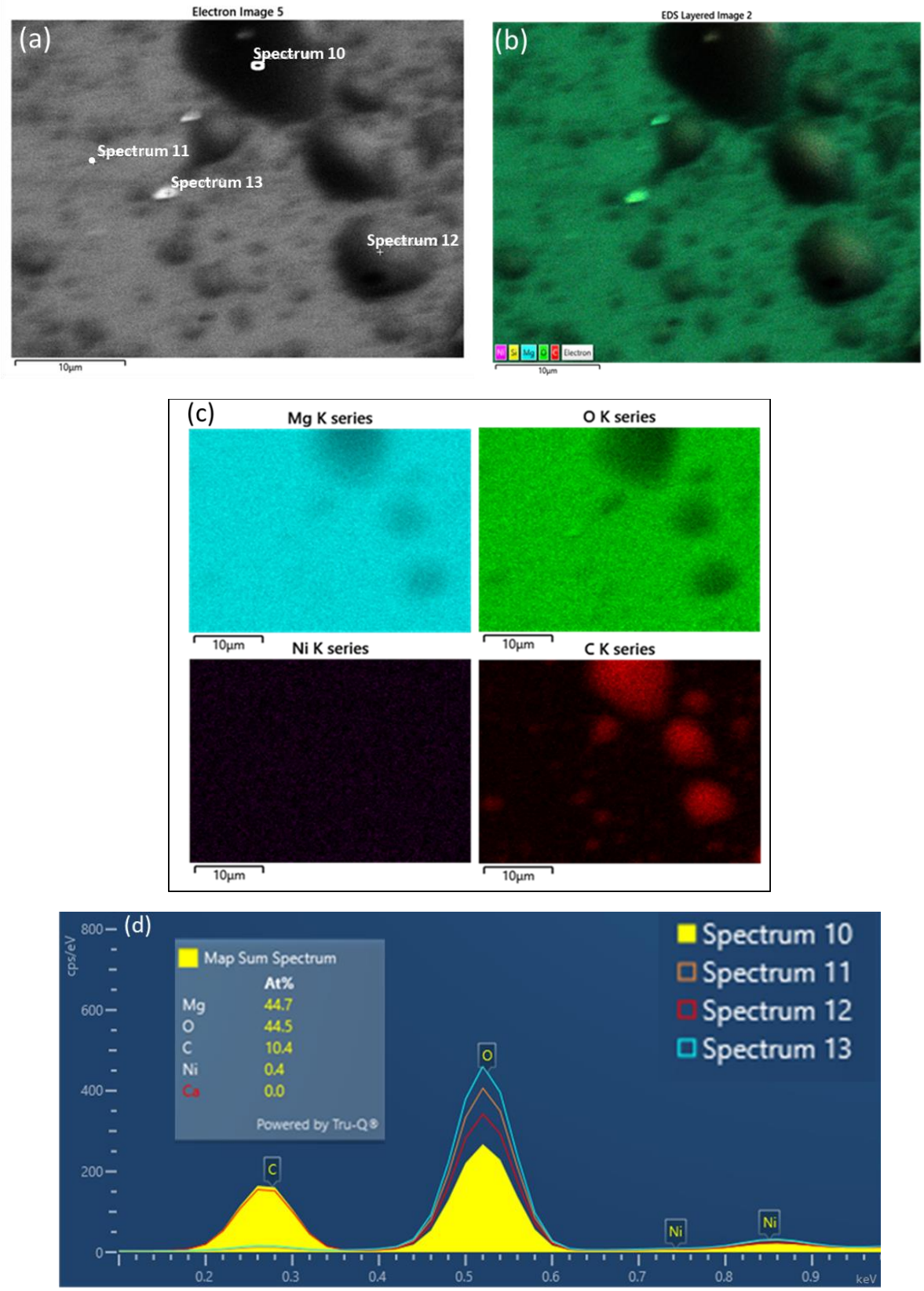

Figure 3. 17: EDS results of Ni on MgO(001) annealed at 400°C showing (a) selected area for mapping and spectrum analysis, (b & c) elemental mapping results confirming the presence of the elements Mg and O from the substrate, Ni from the film and also the presence of C on the surface, (d) spectrum analysis showing the sum spectrum and atomic percentage of each element in the film.

TEM Results

The cross-sectional TEM images of Ni films annealed (20min) at 400°C are shown in Fig 3.18. Unlike Fe films, Ni films do not show definite non-oxidised and oxidised layers of Nickel. The similar contrast between the lower and upper layers is not due to composition but to surface roughness and hence mass/thickness contrast. This indicates a less uniform growth possibly due to the larger mismatch between film and substrate. The interface between the film and substrate (Fig. 3.18 d) seems not planar but has an irregular step-like structure. The film shows the presence of moiré fringes due to the overlapping of grains (Fig. 3.18 c & d) which confirms a polycrystalline growth of Ni.

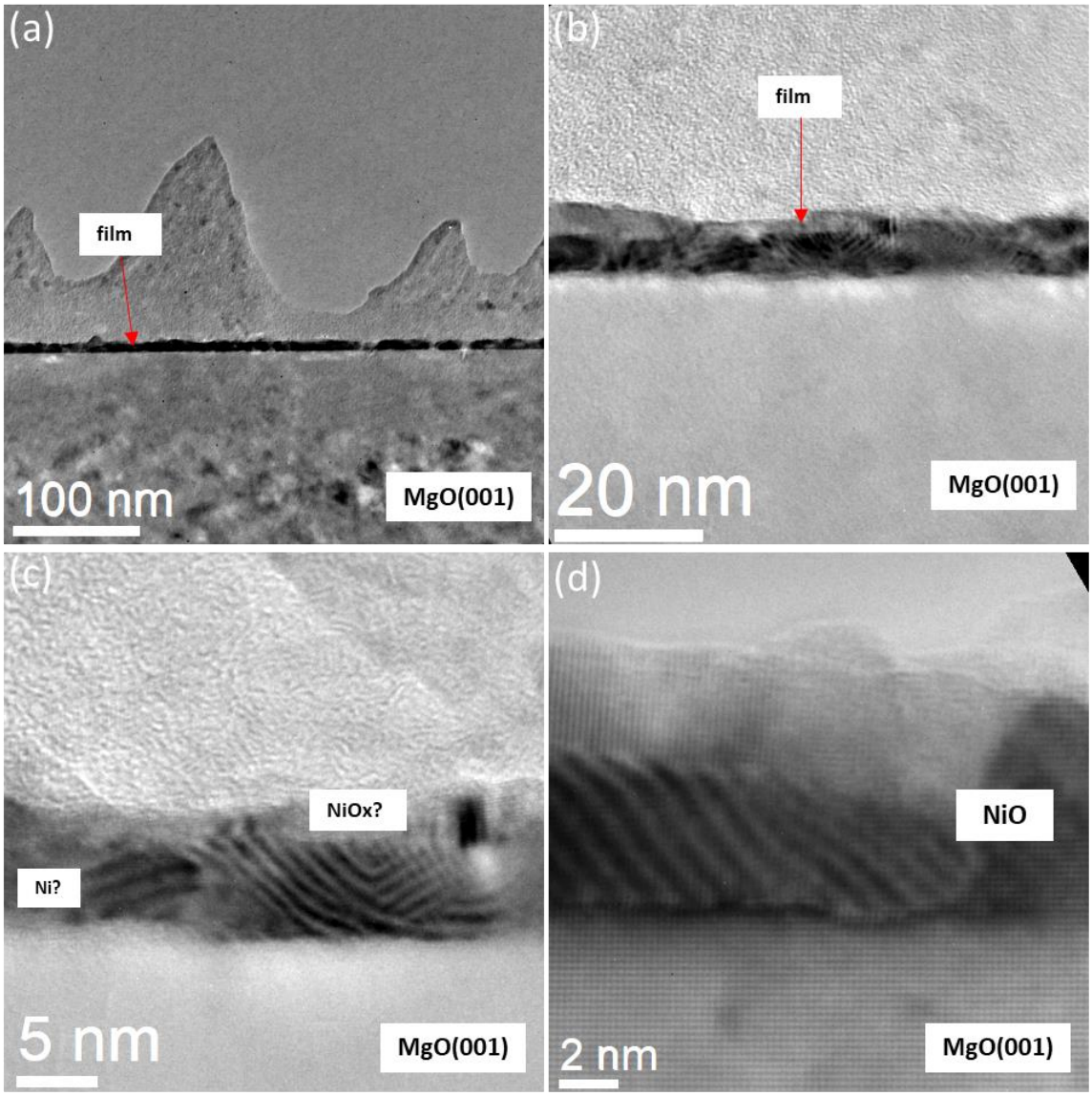

Figure 3. 18: Cross-sectional Bright-Field (BF) low and high magnification TEM images of Ni on MgO(001) annealed for 20 min at 400°C, showing **(a & b)** non-uniform growth of Ni on MgO(001) **(c)**HRTEM image showing the step like interface between the substrate and film and overlapping of grains (moiré fringes), **(d)** HRTEM image showing that the film is fully oxidised.

The lattice d-spacing analysis performed using FFT diffractograms from the HRTEM images (shown in Fig. 3.19) shows that the film is completely oxidised. The FFT results could also be supported by the analysis of the selected area electron diffraction (SAED) pattern using JEMS software (shown in Fig 3.20), and it is clear that the film is totally oxidised because the distances in the reciprocal space correspond to NiO. Although there is an overlapping between Ni and NiO rings of $g_{(111)}$ and $g_{(200)}$, the lack of Ni (200) ring indicates a full oxidation.

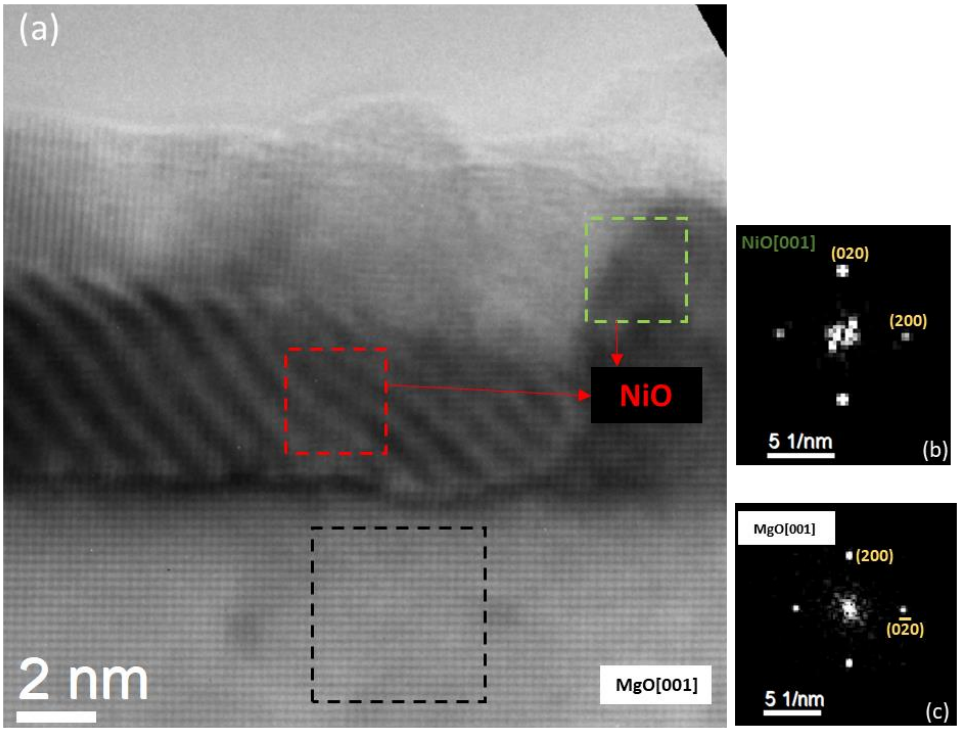

Figure 3. 19: (a) HRTEM image of Ni on MgO(001) annealed at 400°C comprising of area chosen for the lattice d-spacing analysis of substrate MgO (black dashed box), and the film (red and green dashed box); (b) FFT diffractogram of NiO [001]; **(c)** FFT diffractogram of MgO [001].

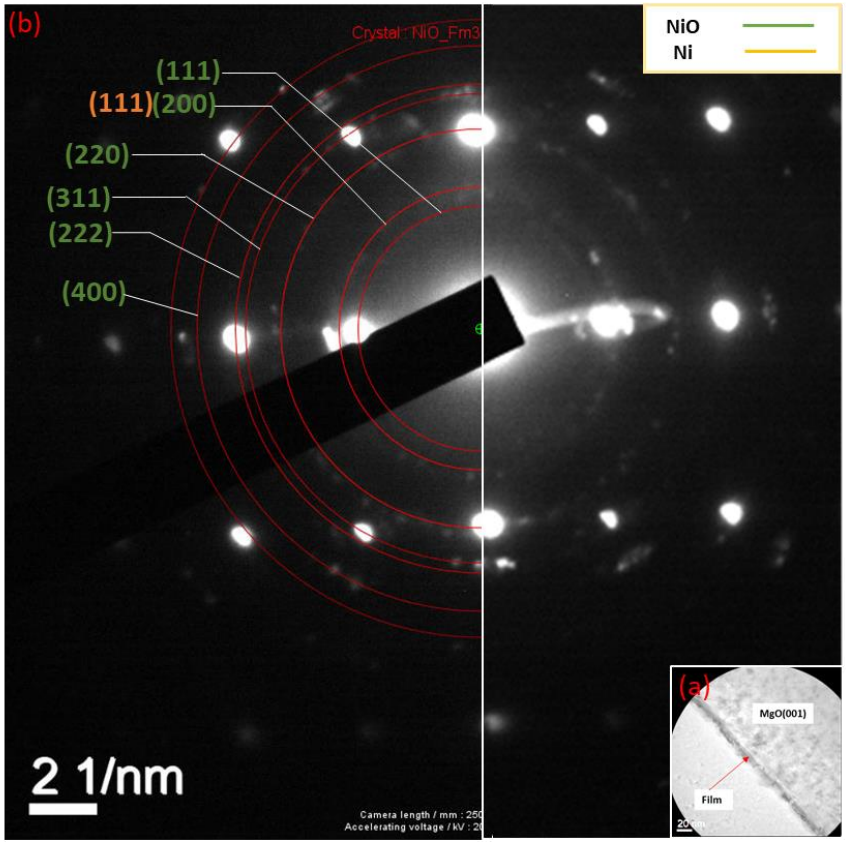

Figure 3. 20: (a) Selected area for the diffraction pattern from the substrate MgO(001) and film; (b) Analysed SAED pattern showing that the Ni film is fully oxidised.

Chapter 4
Conclusion

The epitaxial growth of Fe and Ni films on MgO(001) substrate in this study clearly shows the difference in the growth of single and polycrystalline structures and also helps to understand the impact of annealing on the surface morphology and structure of the films.

The Fe on MgO(001) film in the as-grown condition showed a non-uniform growth with a rough (RMS roughness of 0.91 nm) and stepped surface. While annealed (in situ) Fe film on MgO(001) at 400℃ showed a tremendous change in the surface morphology. The grain growth and film crystallisation caused by annealing resulted in a rise in the surface roughness of the film to 3.30 nm. The TEM analysis proved that the film gets oxidised after annealing and shows good epitaxial and single crystalline growth. The analysis of lattice d-spacing from HRTEM images and SAED pattern could determine the presence of Fe_3O_4 (magnetite) along with non-oxidised iron.

On the other hand, the as-grown Ni film on MgO(001) exhibits a non-uniform and highly rough surface (RMS roughness of 1.61 nm) with a granular structure. The surface of annealed (in-situ) Ni on MgO(001) film at 400℃ seems rougher than the as-grown Ni films. The RMS roughness of 4.61 nm from the AFM analysis indicates that the surface roughness of the Ni samples increased with annealing. The TEM studies showed a less uniform polycrystalline growth of Ni on MgO(001). The lattice d-spacing analysis from the HRTEM images and SAED pattern proved that the film is fully oxidised and the distances in the reciprocal space correspond to NiO.

Overall, the structural studies of Fe and Ni films on MgO showed that the growth of Fe films on the MgO substrate was more uniform than Ni films. Ni films showed more surface roughness compared to Fe films. This is possibly due to the larger mismatch (∼16%) between Ni film and MgO substrate. This study helps to understand that the MBE growth will be better if the crystalline structure and lattice parameter of the layers or deposits are more compatible with the substrate.

4.1 Future work

The lattice mismatch of ∼4% results in a high-quality growth of Fe on MgO(001). On the other hand, the growth of Ni films on MgO(001) seems more challenging due to the lattice mismatch of ∼16% and the results from my studies also support the statement. To make the growth better, the selection of the substrate is important. The YSZ(001) substrates which are more compatible with Ni material

are in consideration. Further, works can include the growth of both Fe and Ni films on YSZ(001). Here the strain would be the opposite i.e., Fe would be having more strain (with a lattice mismatch of ~21%) than Ni (lattice mismatch of ~3%) on YSZ. It is assumed that the strain will influence the dynamics and the size of the oxidised layer. Different rates of oxidation, depending on the crystallographic directions are expected instead of layer-by-layer oxidation in the case of Fe on MgO which can lead to a non-uniform oxide-film interface. In other words, this interface might appear significantly rougher, which likely be also seen as an increase in surface roughness on these films.

In-situ annealing (in the MBE chamber) of Fe and Ni thin films on YSZ can also be done under a controlled oxygen atmosphere at different temperatures. Parameters such as O_2 partial pressure and annealing time can also be varied during annealing. In the case of the Fe thin films, this can produce a variety of different stoichiometry since Fe has two oxidation states that can appear as FeO, Fe_2O_3 and Fe_3O_4, with α-Fe_2O_3 as a ground state. In-situ oxidation of Fe and Ni thin films under a controlled oxygen atmosphere within the aberration-corrected environmental TEM/STEM microscope to study the evolution of the surfaces, defects and strain as a function of time, temperature and oxygen pressure during oxidation is under consideration. The study of the oxidation mechanism, substrate/film and metal/oxide interface microstructure and chemistry by EDS, electron energy loss spectroscopy (EELS) and electron diffraction can also be done.

Another aspect of this research would be studying the magnetic properties of the oxide/metal films (Fe & Ni) for various applications. In the case of Fe/FeO_x, there can be two magnetic distinctive systems, one is ferromagnet metal/ferrimagnetic oxide bilayers, i.e., Fe_3O_4/Fe or γ-Fe_2O_3/Fe. The second type of bilayer is antiferromagnetic oxide/ferromagnetic film. e.g., α-Fe_2O_3/Fe and FeO/Fe. Those interfaces can show interesting ordering including exchange bias. Hence temperature-dependent measurements by VSM (Vibrating Sample Magnetometer) or SQUID/VSM (Superconducting quantum interference vibrating sample magnetometer) would be very useful. In the case of Ni films, since Ni has only 2+ valence only one magnetic bilayer system is expected. An example would be NiO/Ni bilayers, which should show typical AFM/FM behaviour including exchange bias.

The removal of carbon contamination from the surfaces of the film before SEM/EDS and AFM analysis will be considered seriously as it affects my current study. Several measures including cleaning with compatible solvents, plasma

cleaning and optical baking at 80°C in high vacuum will be considered for the removal of any contamination from the films.

References

1. Kakani, A.K.a.S.L., *Material Science*. 2004: New Age International (P) Ltd. 656.
2. Kittel, C., *Introduction to Solid State Physics*. 1953: John Wiley & Sons. 720.
3. Roshini Ramachandran, D.J.A.M.S., *Cross-linking dots on metal oxides.* NPG Asia Materials, 2019.
4. Victor E. Henrich, P.A.C., *The Surface Science of Metal Oxides*. 1994: Cambridge University Press. 464.
5. Fierro, J.L.G., *Metal Oxides: Chemistry and Applications*. 2005: CRC Press. 808.
6. Védrine, J.C., *Importance, features and uses of metal oxide catalysts in heterogeneous catalysis.* Chinese Journal of Catalysis, 2019. **40**(11): p. 1627-1636.
7. V. Palma, C.R., M. Martino, E. Meloni, A. Ricca, *Bioenergy Systems for the Future*. Catalysts for conversion of synthesis gas. 2017: Elsevier. 217-277.
8. Jordi Llorca, V.C.C., Núria J. Divins,Raquel Olivera Fraile,Elena Taboada, *Renewable Hydrogen Technologies*. Chapter 7 Hydrogen from Bioethanol. 2013: Elsevier.
9. Julie Aguilhon a b, C.B.b., Olivier Durupthy b, Cécile Thomazeau a, Clément Sanchez b, *Studies in Surface Science and Catalysis*. Nickel nanoparticles with controlled morphologies application in selective hydrogenation catalysis. Vol. 175. 2010: Elsevier.
10. Shih, H., *Corrosion Resistance*. 2012. 484.
11. Tanzosh, M.J.T.M., *Corrosion resistant nickel oxide surface coating*. 1995, McDermott Technology Inc.
12. M.F. Al-Kuhaili, S.H.A.A., S.M.A. Durrani,M.M. Faiz,A. Ul-Hamid, *Materials Science in Semiconductor Processing*. Application of nickel oxide thin films in NiO/Ag multilayer energy-efficient coatings. Vol. 39. 2015: Elsevier.
13. Anuja Sharma, D.M., Aayushi Arora,Arun Kumar,Chandra Mohan Srivastava,Varun Rawat,Hyunook Kim,Monu Verma,Gyandshwar Kumar Rao, *Green Nanomaterials for Industrial Applications*. Chapter 14 Applications of green nanomaterials in electronic and electrical industries. 2022: Elsevier.
14. A. Venkatanarayanan, E.S., *Comprehensive Materials Processing*. 13.03 Review of Recent Developments in Sensing Materials. Vol. 13. 2014: Elsevier.
15. Xiaoyi Wang, Y.L., Dainan Zhang,Tianlong Wen,Zhiyong Zhong, *A review of Fe3O4 thin films: Synthesis, modification and applications.* Journal of Materials Science & Technology, 2018. **34**(8): p. 1259-1272.
16. I. Hotovy, V.R., P. Siciliano, S. Capone, and L. Spiess, *Sensors for Environmental Control*. NiO thin films for gas sensing applications. 2003.
17. Hotovy, I., *Au-NiO nanocrystalline thin films for sensor application.* Journal of Physics, 2006. **61**.
18. Yakout, S.M., *Spintronics: Future Technology for New Data Storage and Communication Devices.* Journal of Superconductivity and Novel Magnetism, 2020(33): p. 2557–2580
19. Barthelemy, M.B.A., *Oxide Spintronics.* IEEE Transactions on Electron Devices, 2007. **54**(5): p. 1003 - 1023.
20. Anjali Panchwanee, M.K., *Synthesis and Characterization of Vertically Aligned La0.7Sr0.3MnO3:NiO Nanocomposite Thin Films for Spintronic Applications.* ACS Applied Nano Materials, 2021.
21. Takahiro Moriyama, K.O.T.O., *Spin torque control of antiferromagnetic moments in NiO.* Nature, 2018.
22. Thanh Tai Nguyen, M.P., Joondong Kim, *All-inorganic metal oxide transparent solar cells.* 2020. **217**.

23. Goll, G., *Unconventional Superconductors*. Metal-Oxide Superconductors. Vol. 214. 2006: Springer. 121–151.
24. Kassiba, M.M.-J.A.-H., *Handbook of Computational Chemistry* Photoactive Semiconducting Oxides for Energy and Environment: Experimental and Theoretical Insights. 2016: Springer.
25. Yasmin Abdul Wahab, S.F., Muhammad Nihal Naseer,Mohd Rafie Johan,Nor Aliya Hamizi,Suresh Sagadevan,Omid Akbarzadeh,Zaira Zaman Chowdhury,Thennarasan Sabapathy,Y. Al Douri, *Metal Oxide Powder Technologies*. Chapter: 18 Metal oxides powder technology in dielectric materials. 2020: Elsevier.
26. B. Amudhavalli, R.M., M. Prasath, *Synthesis chemical methods for deposition of ZnO, CdO and CdZnO thin films to facilitate further research.* Journal of Alloys and Compounds, 2022. **925**.
27. Hideaki Adachi, K.W., *Handbook of Sputtering Technology*. Chapter: 1 Thin Films and Nanomaterials. 2012: Elsevier.
28. A di Bona, C.G., S Valeri, *Growth and structure of Fe on MgO(001) studied by modulated electron emission.* Surface Science, 2002. **498**(1-2): p. 193-201.
29. J.L Costa-Krämer, J.L.M., A Cebollada,F Briones,D García,A Hernando, *Magnetization reversal asymmetry in Fe/MgO(0 0 1) thin films.* Journal of Magnetism and Magnetic Materials, 2000. **210**(1-3): p. 341-348.
30. Anna L. Ravensburg, G.K.P., Merlin Pohlit,Björgvin Hjörvarsson,Vassilios Kapaklis, *Influence of misfit strain on the physical properties of Fe thin films.* Thin Solid Films, 2022. **761**.
31. Reinke, G.R.P., *Growth of Ni and Ni-Cr alloy thin films on MgO(001): Effect of alloy composition on surface morphology* Journal of Applied Physics, 2016. **120**(22): p. 225-302.
32. J.P McCaffrey, E.B.S., J.R Phillips,L.D Madsen, *Epitaxial variations of Ni films grown on MgO(0 0 1).* Journal of Crystal Growth, 1999. **200**(3-4): p. 498-504.
33. SAHAY, A. *Magnesium Oxide Formula: Structure, Properties, Reactions*. 2023; Available from: https://www.embibe.com/exams/magnesium-oxide-formula/.
34. Zhihao Pan, C.Y.Z., *Dehydration/hydration of MgO/H2O chemical thermal storage system.* Energy, 2015. **82**: p. 611-618.
35. Hillier, K., *xPharm: The Comprehensive Pharmacology Reference*. Magnesium Oxide. 2007: Elsevier.
36. Werner Pepperhoff, M.A., *Constitution and Magnetism of Iron and its Alloys*. 1 ed. Engineering Materials. 2001. 226.
37. J. M. D. Coey, M.V., Hongjun Xu, *Functional Metal Oxides: New Science and Novel Applications*. Chapter9: Introduction to Magnetic Oxides. 2013.
38. Meena, C., *Stability of Transition Metal Complexes Halides of the Nickel Metal.* International Journal of Trend in Scientific Research and Development (IJTSRD), 2022. **6**(6): p. 99-105.
39. K.O. Ukoba, A.C.E.-E., F.L. Inambao, *Review of nanostructured NiO thin film deposition using the spray pyrolysis technique.* Renewable and Sustainable Energy Reviews, 2018. **82**: p. 2900-2915.
40. Chambers, A.S., *Modern vacuum physics*. 2004: Taylor & Francis group.
41. Ohring, M., *Materials Science of Thin Films*. 2002, Academic Press, San

Diego.
42. David B. Williams, C.B.C., *Transmission electron microscopy*, in *A Textbook for Materials Science*. 2009, Springer New York, NY. p. 775.
43. Hans H. Gatzen, V.S., Jürg Leuthold, *Micro and Nano Fabrication*, in *Tools and Processes* 2015.
44. Alp T. Findikoglu, D.E.P.S.T.P., *Epitaxial growth.* Nature, 2011.
45. Henini, D.M., *Molecular Beam Epitaxy From Research to Mass Production*, ed. M. Henini. 2018: Elsevier. 788.
46. HASEGAWA, S., *Characterization of Materials*

Reflection High-Energy Electron Diffraction. 2012: The University of Tokyo.
47. Germer, C.D.a.L.H., *Diffraction of Electrons by a Crystal of Nickel.* Physical Review, 1927. **30**(6).

48. Broglie, L.D., *Research on the theory of quanta.* Annales de Physique 1925. **10**(3): p. 22 - 128.
49. David B. Williams, C.B.C., *Transmission Electron Microscopy, A Textbook for Materials Science*. 2009, Springer New York, NY. p. 775.
50. X Zhou, G.E.T., *Reference Module in Materials Science and Materials Engineering*. Electron and Photon Based Spatially Resolved Techniques. 2017: Elsevier.
51. Kogure, T., *Developments in Clay Science*. Chapter 2.9 Electron Microscopy. Vol. 5. 2013: Elsevier.
52. Ghasemi, A., *Atomic structure of thin films and heterostructure of Bi2Te3 and Bi2Se3 topological insulators*, in *Materials Science*. 2017.
53. Nanakoudis, A., *What is SEM? Scanning Electron Microscopy Explained*. 2019.
54. Akhtar, K., Khan, S.A., Khan, S.B., Asiri, A.M, *Handbook of Materials Characterization*. Scanning Electron Microscopy: Principle and Applications in Nanomaterials Characterization. 2018: Springer.
55. Goldstein, J., *Scanning Electron Microscopy and X-Ray Microanalysis* 3ed. Geochemical Instrumentation and Analysis. 2003. 689.
56. Nanakoudis, A., *EDX Analysis with SEM: How Does it Work?* 2019.
57. Associates, M., *Tech Notes*.
58. G. Binnig, C.F.Q., and Ch. Gerber, *Atomic Force Microscope.* Physical Review Letters, 1986. **56**(9).
59. Sivarajah, I., *Atomic Force Microscopy: General Principles and Applications.* AZoOptics, 2021.
60. Anna L. Ravensburg, G.K.P., Merlin Pohlit,Björgvin Hjörvarsson,Vassilios Kapaklis, *Influence of misfit strain on the physical properties of Fe thin films.* Thin Solid Films, 2022. **761**: p. 139-494.
61. J.P McCaffrey, E.B.S., J.R Phillips,L.D Madsen, *Epitaxial variations of Ni films grown on MgO(001).* Journal of Crystal Growth, 1999.
62. G. Raatz, J.W., *Structure of metal deposits on ceramic materials studied in the Ni/MgO system.* physica status solidi, 1989. **113**(1): p. 131-141.
63. H. Qiu, A.K., H. Maruyama,M. Adamik,G. Safran,P.B. Barna,M. Hashimoto, *Epitaxial growth, structure and properties of Ni films grown on MgO(100) by d.c. bias sputter deposition.* Thin Solid Films, 1994.
64. Hisashi Nakai, H.Q., Miklós Adamik,György Sáfran,Péter B. Barna,Mituru Hashimoto, *RBS and XHRTEM characterization of epitaxial Ni films prepared by biased d.c. sputter deposition on MgO(001).* Thin Solid Films, 1995.
65. Binbin Chen, Z.J., Stefan Abel, Phu Tran Phong Le, Ufuk Halisdemir, Mark Smithers, Daniel Diaz-Fernandez, Matjaž Spreitzer, Jean Fompeyrine, Guus Rijnders, and Gertjan Koster, *Integration of Single Oriented Oxide Superlattices on Silicon Using Various Template Techniques.* Applied Material Interfaces, 2020.
66. Felix V. E. Hensling, D.D., Prabin Dulal, Patrick Singleton, Jiaxin Sun, Jürgen Schubert, Hanjong Paik, Indra Subedi, Biwas Subedi, Gian-Marco Rignanese, Nikolas J. Podraza, Geoffroy Hautier, Darrell G. Schlom, *Epitaxial stannate pyrochlore thin films: Limitations of cation stoichiometry and electron doping* Applied Physics Letters, 2021.
67. Weber, R., *Operando X-ray Diffraction Study of Polycrystalline and Single-Crystal LixNi0.5Mn0.3Co0.2O2.* Journal of The Electrochemical Society, 2017.
68. M. Navasery, S.A.H., N.Soltani, G.Bahmanrokh, A.Dehzangi, M.Erfani H, A.Kamalianfar, S.K.Chen and K.Y.Pan, *High Curie Temperature for La 5/8 Sr 3/8 MnO 3 Thin Films Prepared by Pulsed Laser Deposition on Glass Substrates.* International Journal of Electrochemical Science, 2013. **8**: p. 467 - 476.